Nickel and its isotopes in organic-rich sediments: implications for oceanic budgets and a potential record of ancient seawater

Author(s):
Ciscato, Emily R.; Bontognali, Tomaso R.R.; Vance, Derek

Publication date:
2018-07-15

Permanent link:
https://doi.org/10.3929/ethz-b-000268588

Originally published in:
Earth and Planetary Science Letters 494, https://doi.org/10.1016/j.epsl.2018.04.061

Funding acknowledgement:
143262 - The development and application of transition metal isotope systems in surface Earth geochemistry (SNF)
165904 - Metal isotope constraints on biosphere-environment interactions in Earth history (SNF)

Nickel and its isotopes in organic-rich sediments: implications for oceanic budgets and a potential record of ancient seawater

Emily R. Ciscato[a,*], Tomaso R. R. Bontognali[a,b], Derek Vance[a]

[a] *Institute of Geochemistry and Petrology, Department of Earth Sciences, ETH Zürich, Clausiusstrasse 25, 8092 Zürich, Switzerland*

[b] *Space-X, Fbg de l'Hôpital 68, 2000 Neuchâtel, Switzerland*

Abstract

Nickel (Ni) is a biologically active element that displays a nutrient-like depth distribution in the modern oceans. Recent studies of Ni isotopes have highlighted the fact that, in common with many other transition metals, the Ni stable isotope composition, expressed as δ^{60}Ni, of the dissolved phase is heavier than the inputs, at +1.3 to +1.7 ‰. The sedimentary outputs that control the high δ^{60}Ni of the ocean, coupled with records for past seawater, could potentially yield new information on the past Earth system, but these are currently not well understood. Here we present the first Ni abundance and isotope data for a key output, that associated with Ni uptake into organic matter, at productive upwelling regions and elsewhere. We investigate the distribution of Ni and its isotopes in two fractions separated from the bulk sediment, an HF-digestible fraction, extracted with HF-HCl, and an organic-sulphide-rich fraction. The organic-sulphide fractions exhibit a range in δ^{60}Ni, from +0.86 to +1.83. Systematic relationships between Ni concentrations, total organic carbon and Ni isotopes suggest that the organic-sulphide fraction originates in the photic zone, and is delivered to the sediment as a closed system, despite the possibility of transfer of Ni to sulphide within it. Authigenic Ni in the bulk sediment is dominated by the HF-digestible fraction which, in Ni-enriched sediments where the detrital correction is small, is very close to the modern deep ocean, at δ^{60}Ni = +1.2 ‰. These data

*Corresponding author, E-mail address: emily.ciscato@erdw.ethz.ch (E. R. Ciscato)

suggest that organic-rich sediments beneath upwelling zones, while they are an important output flux of Ni from the oceans, do not solve the isotope balance problem because their δ^{60}Ni is almost identical to modern seawater. On the other hand, the approach adopted here involving the analysis of the two fractions, both traces the fractionation imparted by biological uptake as well as recording the δ^{60}Ni of contemporary seawater, suggesting potential for understanding the past oceans.

Keywords: Nickel, nickel isotopes, organic-rich sediment, authigenic enrichment, Peru margin, Lagoa Salgada

---

1. Introduction

Nickel (Ni) is a bioessential trace metal, characterized by a nutrient-type depth profile in the modern ocean, with dissolved Ni concentrations reaching 11 nM in the deep Pacific and values as low as 2 nM in many parts of the photic zone (e.g., Sclater et al., 1976; Bruland, 1980; Mackey et al., 2002; Lai et al., 2008). The role of biological processes in the oceanic cycling of Ni is confirmed by strong correlations between Ni concentrations and those of the major nutrients like phosphate and silica (Sclater et al., 1976; Bruland, 1980). The specific biological roles of Ni have been reviewed by Ragsdale (2009). Nickel is an essential component of at least seven enzymes involved in the biological cycling of carbon, nitrogen, and sulphur. A further two are of key importance for the metabolism of methanogens, which may have played a prominent role on the early Earth (e.g., Kasting, 2005; Konhauser et al., 2009).

In addition to its clear biological cycling, there are two other important processes that control the marine geochemistry of Ni. First, like many other transition metals, sorption to particulate Fe-Mn oxides represents an important output from the dissolved pool in settings where oxygen is plentiful (e.g., Shaw et al., 1990; Peacock and Sherman, 2007; Gall et al., 2013). On the other hand, Ni is also highly reactive towards dissolved sulphide (e.g., Landing and Lewis, 1991). Thus, in the deep Black Sea sulphidation of dissolved Ni, coupled to either scavenging of particle reactive sulphidised species or to sulphide precipitation, also removes it from solution to sediment (e.g., Landing and Lewis, 1991; Vance et al., 2016).

These aspects of the oceanic Ni cycle represent different outputs from the oceanic dissolved pool - uptake into cells and burial of organics, sorption to Fe-Mn oxides and sedimentation under oxidising conditions, removal to particulate sulphide and sedimentation under reducing conditions - whose relative importance now and in the past is controlled by key aspects of the Earth's surface environment, including biological productivity and

oceanic redox state. Previous work has highlighted the utility of metal isotope studies in quantifying both the relative importance of these sinks in the modern ocean (e.g., Siebert et al., 2003; Little et al., 2014; Andersen et al., 2014), and for understanding the environmental drivers of fluctuations in these sinks throughout Earth history (e.g., Arnold et al., 2004; Pons et al., 2013). For nickel, isotope data published to date for the oceanic dissolved pool (Fig. 1, Cameron and Vance, 2014; Takano et al., 2017) show two key features. Firstly, the δ^{60}Ni (defined as $[(({}^{60}Ni/{}^{58}Ni_{sample})/({}^{60}Ni/{}^{58}Ni_{NISTSRM986})) - 1] * 1000$) of the water column is relatively homogeneous, though there is a subtle shift towards heavier Ni isotopes as Ni is drawn down in the photic zone (Archer et al., 2017; Takano et al., 2017). Secondly, the nickel isotope composition of the dissolved pool is significantly heavier than the main input, the dissolved load of rivers, itself heavier than the best estimate of the upper continental crust (UCC; Cameron and Vance, 2014; Gueguen et al., 2013). This latter feature is common to a number of transition metals (e.g., Arnold et al., 2004; Little et al., 2014), and requires that: (a) the oceans are not in steady-state for Ni and its isotopes; (b) there is an uncharacterized heavy input that dominates over rivers or; (c) that the outputs from the dissolved pool are isotopically light.

The first two potential explanations remain possible, though evidence has been previously marshaled against them (Gall et al., 2013; Cameron and Vance, 2014; Gueguen et al., 2016), and we return to this issue in the discussion in the light of new data presented in this study. Here, we focus on the third possible explanation for the apparent imbalance in the marine isotope budget of Ni. Two outputs from the dissolved pool have been characterized for Ni isotopes. The first is that associated with particulate Fe-Mn oxides (Gall et al., 2013; Gueguen et al., 2016), whose surface layers cluster between δ^{60}Ni=+1.6 and +1.9, with most (n = 22 out of 26) heavier than the modern water column. This finding thus worsens the isotopic mass balance problem (Fig. 1). Secondly, isotopically light Ni is preferentially removed to sediment in sulphidic basins like the Black Sea (Vance et al., 2016). This finding is consistent with the reactivity of Ni towards dissolved sulphide (e.g., Landing and Lewis, 1991), the fact that such aqueous sulphide species are particle reactive

(or perhaps precipitated as sulphide minerals), and that aqueous sulphide species prefer the light isotopes of Ni (Fujii et al., 2014).

Extraction of light Ni from seawater in euxinic water columns is important to the oceanic isotope budget, but this output is almost certainly insufficient to quantitatively solve the balance problem. Here, we quantify a sink that has not yet been characterised for Ni isotopes, but that is well known to be a major output flux of Ni from the dissolved pool of the oceans (Böning et al., 2015) – that associated with cellular uptake in the photic zone and enhanced organic matter preservation beneath productive upwelling zones. In addition, we investigate the degree to which the contemporary seawater signal can be extracted from organic matter in sediments, not only in the organic-rich sediments deposited beneath productive upwelling zones, but also in organic-lean sediments such as carbonate. In contrast to traditional bulk sediment digests, we measure Ni abundance and isotope composition in an HF-dissolvable fraction and an "organic matter plus pyrite" fraction, with the aim of learning more about the location and isotope composition of different isotopic pools of Ni within sediments.

2. Setting

2.1. ***Peru Margin***

The Peru Margin was chosen as the principal focus for this study, as it offers the opportunity to investigate organic-rich sediments deposited at sites with a range of bottom-water oxygen (O_2) concentrations, and thus different sedimentary redox states. The Peru-Chile margin is considered as the most productive upwelling system in the world ocean (Fuenzalida et al., 2009). The high productivity of this region results in the permanent eastern South Pacific oxygen minimum zone (OMZ), which has its core located between 5 and 13°S. The seafloor below the OMZ and along the margin is dominated by two main sedimentary facies: (i) a lens-shaped, up to 100m thick, diatomaceous (opal up to ∼16 wt.%), organic-rich mud at depths between 50 and 500m at 11-14°S; and (ii) a coarser-grained, less organic-rich, calcareous mud on the shallow shelf at 8.5°S and 15-17°S (Suess

et al., 1987). Thus, the most organic-rich sediments are deposited between 11 and 14°S, which are the latitudes targeted here.

Peru Margin sediment cores were recovered as box cores and multicores in October-November 1992 during a cruise of *R/V Seward Johnson*, and as multicores in October-November 2005 during cruise 182-9 of *R/V Knorr*. Upon recovery, all cores were immediately sliced at 0.5-1.0cm intervals, stored in glass jars or plastic sampling bags, and frozen. In this study we focused on core-tops recovered by *R/V Seward Johnson* and multiple down-core samples from three of the cores recovered by *R/V Knorr* (Fig. 2a,b), in order to cover a range of redox conditions and organic matter contents. Following Böning et al. (2004), the samples can be subdivided into three groups based on their location with respect to the OMZ (see Supplementary Information for precise locations): (i) upper edge of the OMZ, where O_2 is recorded to be $<10\mu$M but may fluctuate to higher values during El Niño years; (ii) lower shelf and upper slope, within the OMZ where O_2 is at or below 5μM; (iii) lower continental slope, below the OMZ.

2.2. ***Lagoa Salgada***

The Lagoa Salgada site was chosen to investigate whether its carbonate-rich (34-75%) sediments, although only moderately organic-rich, also offer the possibility for isolating an authigenic fraction. Lagoa Salgada is a coastal lagoon located south of the mouth of Rio Paraíbo do Sul, in the south-east of Brazil (Fig. 2a,c), connected to the Atlantic Ocean via the tidal channel Rio Acu (Bovier, 2015). Water depth and salinity are variable depending on the season; the maximum depth, however, is mostly <1m. The sediments are carbonate-rich, with minor pyrite (Bovier, 2015).

Sampling took place in July 2014, when a sediment core was taken from the south-western shore of the lagoon by immersion in the sediment of a polyvinyl chloride (PVC) tube. The core was then sampled at 1.0cm intervals and frozen.

3. Methods

Much of the analytical methodology used in this study has been documented before (Cameron et al., 2009; Cameron and Vance, 2014; Vance et al., 2016). The details are recapitulated in the Supplementary Information, with only a brief summary given here. However, the two-step digestion approach we use here is new. This is described in more detail in section 3.1 below, and further relevant data are also presented in the Supplementary Information.

One of our aims here was to investigate the location and isotope composition of Ni in different fractions of organic-rich sediment, specifically those in an HF-digestible fraction versus a residual organic matter-rich fraction. Our approach was inspired by previous studies aimed at extracting kerogen from ancient organic-rich samples for carbon isotope analysis (Eigenbrode and Freeman, 2006). Around 1g of bulk sediment was subjected to a HF-HCl digestion for 24hr followed by two steps involving 24hr reflux with 7M HCl, evaporating to dryness between each step. Following re-dissolution in 7M HCl, the resulting HF-dissolvable fraction (HFD) and the residual solid (organic matter and associated pyrite, OPF) were separated by centrifugation and decanting of the supernatant solution. The residual OPF was brought into clear solution via high-pressure ashing (HPA-S by Anton Paar) in a 10:1 mixture by volume of 13M HNO_3 and 10M HCl. Tests we describe below and in the Supplementary Methods strongly suggest that small sulphide grains that are intimately associated with organic matter are not significantly attacked by the initial HF-HCl treatment. We are not able to be sure, at this stage, whether Ni from larger sulphide grains that may be present in the samples and that are not intimately-associated with organic matter, is mobilised by the HF-HCl fraction.

All OPF and HFD fractions were analyzed for elemental abundances on a ThermoScientific Element XR^{TM} inductively-coupled plasma mass spectrometer (ICP-MS) at ETH Zürich. Nickel was then separated from the matrix by column chromatography following

the addition of a double spike for the monitoring of mass bias. The total Ni blank for this procedure was 3ng, dominated by the DMG column. A blank correction was applied to all samples assuming a δ^{60}Ni for the blank of 0. For all except one sample, the resulting shift is no greater than analytical uncertainty (for LS30 OPF δ^{60}Ni is shifted upwards by 0.15 relative to that with no blank correction). Nickel isotopic compositions were measured on a ThermoFinnigan NeptunePlus multicollector ICPMS at ETH Zürich, and are reported relative to the NIST SRM986 standard, according to the following notation:

$$\delta^{60}Ni = \left[\frac{^{60}Ni/^{58}Ni_{sample}}{^{60}Ni/^{58}Ni_{NISTSRM986}} - 1 \right] * 1000 \quad (1)$$

The long-term external reproducibility was determined by repeat measurements of two secondary standards, USGS NodA1 and Nod P1. Analyses performed during the period when the data presented here were obtained yielded $\delta^{60}\mathrm{Ni} = 1.04 \pm 0.07$ ‰ (n = 120) and $\delta^{60}\mathrm{Ni} = 0.34 \pm 0.08$ ‰ (n = 99), respectively. In all tables and diagrams, these reproducibilities are taken to be the real uncertainties unless, as in rare cases when analytical signals were small, the internal uncertainty was greater, in which case the latter is used.

Freeze-dried bulk sediment samples and the extracted OPF were also analyzed for total organic carbon (TOC) and δ^{13}C. Details are also provided in the Supplementary Information. Isotope ratios are reported in the conventional notation with respect to the V-PDB (Vienna Pee Dee Belemnite) standard:

$$\delta^{13}C = \left[\frac{^{13}C/^{12}C_{sample}}{^{13}C/^{12}C_{V-PDB}} - 1 \right] * 1000 \quad (2)$$

3.1. ***Tests of the two-step digestion methodology***

We have conducted extensive tests to investigate the degree to which the two separate fractions might exhibit chemical and isotopic artefacts due to the two-step digestion. For example, it is possible that some of the organic matter contained in the samples is extracted through the initial HF-HCl digestion. Figure 3 presents TOC data for the bulk sample, measured before any HF-HCl treatment, and compares it with the TOC content of the OPF, obtained after the HF-HCl digestion. Clearly the data fall on a reasonably narrow array, with the solid line on Figure 3 implying 90% retention of the organic carbon in the OPF after the HF digestion. We also measured δ^{13}C in selected bulk samples for the Peru Margin as well as the OPF (Table 1), in order to test for any isotope fractionation during the HF-HCl digestion. The two datasets show the same range: -22.2 to -20.2 in the bulk sample versus -22.2 to -20.3 in the OPF. For individual samples, the two measurements are in most cases analytically identical, with the maximum difference between the two being 1.2‰.

Clearly, the extraction of organic carbon in the residual OPF is close to complete and there is no isotopic artefact for carbon associated with the HF treatment. Tests of whether the Ni inventory in the OPF fraction extracted corresponds to the original equivalent in the bulk sample are more difficult, because the HF-digestible fraction itself contains substantial Ni. There are several potential issues: (1) is the OPF fraction contaminated by un-digested silicate material, such as clays; (2) is Ni preferentially extracted from the OPF relative to, e.g., carbon; (3) is there isotope fractionation of Ni associated with such removal? There are small amounts of Al (Table 1) and other elements (see Supplementary Information) associated with the OPF, but element ratios do not correspond to those of clay minerals and XRD analysis demonstrates that the Al in the OPF, and other elements like Na, is rather associated with residual fluoride salts (see Supplementary Information). We investigated the potential issue of preferential leaching of Ni, or its isotopes, using three subsamples of a Peru Margin core-top. The different subsamples were subjected to either one, two, or three separate HF treatments, all of which were analyzed, and after

which the residual OPF fraction was ashed and analyzed. The results are presented in detail in the Supplementary Information but to summarize here: (1) the amount of Ni extracted by a second or third HF treatment is $\leq$10% that of the first treatment; (2) the δ^{60}Ni of the resultant HFD fractions are within analytical uncertainty of each other; (3) the Ni concentrations in the OPF after one, two, or three HF treatments are analytically identical and; (4) the δ^{60}Ni of the different OPF fractions are within analytical uncertainty of each other.

Though we acknowledge that our attempt to separate the HF-digestible Ni fraction from that in organic material cannot be shown to be perfect, we suggest that these tests constitute strong evidence that it was for the most part successful. We further address the degree to which the OPF remains a relatively closed system, not only during digestion but also in the water column and sediment after Ni is first taken up by organic matter, in section 5.1.

4. Results

4.1. ***Peru Margin***

The Peru Margin samples have TOC contents of 1.6-14.2 wt.% (Table 1), which is within the range reported by previous studies for sediments from the same area (Böning et al., 2004). As previously suggested by Böning et al. (2004), the systematic increase in TOC contents from sites beneath the OMZ to those deposited within it (Table 1) probably results mainly from a combination of enhanced organic matter preservation in more O_2-limited settings, but also from reduced supply of organic matter in deeper settings, and different extents of its poleward transport by the undercurrent. Carbon isotope analyses of the extracted OPF fractions yield a narrow range of δ^{13}C: -20.3 to -22.2 ‰ (Table 1). These values are indicative of organic matter that is predominantly of marine origin, in agreement with previous studies from this specific area (e.g., Calvert and Price, 1983).

4.1.1. ***Ni concentrations and isotopic composition of modern organic-rich sediments***

Ni concentrations and isotopic compositions for the bulk (Fig. 4a) and the individual HFD and OPF fractions (Fig. 4b) are presented in Table 1. Overall, the abundance of Ni in the bulk samples follows the same general pattern as that reported by Böning et al. (2004), who observe that Ni is most abundant in samples collected from within the OMZ, while lower concentrations are found in samples from the upper edge and below the OMZ. Ni in bulk samples is 18-139 ppm, with the respective HFD fractions containing 17-113 ppm and the OPF fractions 0.8-26 ppm. For all samples, most of the Ni is in the HFD fraction (70 - 96 %). There is no systematic change in Ni concentrations down core, in either the two fractions or in the bulk samples. The lowest Ni concentrations are always observed in samples from the most oxic setting, core MC9G (bulk: 18 - 22 ppm, HFD: 17 - 19 ppm, OPF: 0.8 - 2.7 ppm), whereas Ni is most abundant in core MC11C, from within the OMZ (bulk: 82 - 139 ppm, HFD: 66 - 113 ppm, OPF: 16 - 26 ppm). Core MC6A, as well as the core-tops from the upper OMZ and below the OMZ, lie between these, with Ni concentrations of 31 - 50 ppm for the bulk, 25 - 42 ppm for the HFD, and 5.6 - 15 ppm for the OPF. The cores are also significantly different in terms of the percentage of total Ni contained in the HFD fraction: 70 - 80 % for core MC6A versus 80 - 83 % for core MC11C and 87 - 96 % for core MC9G.

The bulk δ^{60}Ni for all samples lies in the range +0.94 to +1.33, close to or below the average δ^{60}Ni of the modern deep ocean (Fig. 4a). The OPF fractions exhibit the greatest isotopic variation, between +0.86 and +1.83, with the heaviest values observed in samples from core MC6A and the lightest in samples from core MC11C (Fig. 4b). The HFD fractions have δ^{60}Ni compositions between +0.86 and +1.37, hence also close to or below the average value for the modern deep ocean δ^{60}Ni (Fig. 4b).

4.2. ***Lagoa Salgada***

The TOC content of Lagoa Salgada sediments is mostly homogeneous below 20 cm down-core (between 2.1 and 3.4 wt.%). Carbon isotopes show a larger range than for Peru (-7.0 to -23.5). This, and the fact that the $\delta^{13}C_{organic}$ values reported here show a relatively constant shift from $\delta^{13}C_{carbonate}$ (Bovier, 2015) of 24.6 ± 1.2 ‰, suggests a reservoir effect affecting carbon isotopes in the lagoon.

4.2.1. ***Ni concentrations and isotopic composition of Lagoa Salgada carbonate-rich sediments***

Apart from one very anomalous sample at 66 cm, Lagoa Salgada sediments have Ni abundances of <4 ppm (bulk: 2.0 - 3.9 ppm, HFD: 1.8 - 3.6 ppm, OPF: 0.07 - 0.31 ppm, Table 1). The δ^{60}Ni of the calculated bulk sediment, and of the HFD, are +0.17 to +0.31 ‰, with the exception of one bulk sample from 15 cm sediment depth in the core which is heavier at +0.71 ‰(Table 1). The extracted OPF fraction, on the other hand, seems to record the δ^{60}Ni of the modern average deep ocean, with the exception of two samples, at 15 and 30 cm sediment depth, that are very slightly heavier (Table 1).

5. Discussion

5.1. ***The source of Ni in Peru Margin organic-rich sediments***

Böning et al. (2015) have previously identified a single strong correlation (with a near zero intercept) between measured [Ni] and TOC, for organic-rich sediments in upwelling regions globally. They also noted that Ni in the surface layers (0 - 2 cm) was dominantly associated with chlorins, the immediate degradation products of chlorophyll pigments. Overall, these findings led Böning et al. (2015) to conclude that the dominant control on Ni abundances in organic-rich sediments was the supply of organic matter photosynthesised by diatoms. As highlighted in Figure 5a the data presented here for Peru Margin sediments reproduce these findings of Böning et al. (2015). Down-core [Ni] and TOC data, irrespective of the location of the core with respect to the OMZ, lie on the array

defined by the Böning et al. (2015) dataset.

One important question that arises here is the extent to which the Ni content of phytoplankton cells, as measured in the photic zone, is quantitatively sufficient to explain sedimentary Ni/TOC relationships. The slope of the array in Figure 5a is about $9*10^{-4}$ g/g or 180 μmol/mol. By contrast, reported Ni/C ratios in diatom cells are 4 - 8 μmol/mol (Twining et al., 2011, their Table 5 and equivalent to a Ni/P ratio of 1.2 mmol/mol), with Ni in diatoms distributed roughly equally between internal biomass and frustule (Twining et al., 2012). Thus, at face value, only a few % of the total Ni in Peru Margin sediments can be explained by incorporation of Ni into diatom cells and the unmodified export of these cells to the sediment.

As shown in Figure 5c, the data for the organic-pyrite fraction (OPF) also imply a reasonably constant Ni/C ratio for Peru Margin samples, with most of the data between 2 and $4*10^{-4}$ g/g or 40-80 μmol/mol, equivalent to a Ni/P ratio of 4 - 8 mmol/mol for a Redfield C/P ratio. Data for phosphorous in the OPF, shown in Figure 5d, also suggest a very constant Ni/P ratio, with the exception of two outlying OMZ samples that are anomalously enriched in P. The Ni/P ratio implied by this correlation is much greater, at about 90 mmol/mol. However, the C/P implied by the P data is also much higher than the Redfield ratio, most likely due to the preferential remineralization of P that is well-known in organic-rich sediments (e.g., Ingall and Jahnke, 1994; Paytan and McLaughlin, 2007). These findings lead us to put forward a hypothesis, one that can potentially be tested with isotope measurements: that the Ni in the organic-pyrite fraction we extract from these sediments may represent a reservoir that is sequestered to cells in the photic zone, and that is transferred in relatively unmodified form to Peru Margin sediment.

The Ni/P in the OPF implied by the Ni/C data and Redfield C/P is greater than that previously found for the organic matter in single diatom cells recovered from the photic zone (0.52 ± 0.10; Twining et al., 2012), but overlaps with the range for the bio-

genic fraction of both mixed layer (0.54 - 3.6) and ODZ particulates (4.6 - 4.8) reported in Ohnemus et al. (2016). Though these latter authors present compelling evidence for the presence of prokaryotic organisms, as opposed to diatoms, associated with particulate maxima just beneath the mixed layer, at 50 - 250m, there is a second potential explanation of the metal/P data in sub-surface particulates. Secondary electron microscope images (see Supplementary Information) of the OPF extracted from the samples studied here demonstrate that they contain two intimately associated phases – organic matter and very small sulphide grains. An alternative interpretation of the data in Ohnemus et al. (2016) is that the metal/P ratios of the particulates recovered from 50 - 250m, with Ni/P ratios up to 4.8, represent those associated with decaying diatom organic matter from the mixed layer. In other words, it is possible that these particulates represent diatom cells that have lost carbon and phosphorus due to respiration while retaining metals like Ni, perhaps in sulphide grains. The suggestion that metals are sequestered in reducing micro-environments around decaying organic matter has been made before for other metals (e.g., Cd, Zn; Janssen et al., 2014; Janssen and Cullen, 2015).

In either case - modified diatom organic matter from the mixed layer or modified prokaryotic organic matter from the deeper part of the photic zone - the consistency in relationships between Ni, P and carbon found here could be taken to suggest that the Ni in the OPF derives from the upper 250m of the water column, with some loss of carbon and phosphorus to respiration. The OPF fraction would then have to remain a pseudo-closed system for Ni - through the water column, into the sediment, and during the extraction process by which we isolated it here. This hypothesis has caveats too. For example, only $17 \pm 6\%$ (1SD) of the authigenic Ni (see corrections for detrital Ni in section 5.3) in the bulk sediments analyzed here is contained in the OPF, with the remainder in the HF-digestible fraction. This opens the difficult question of where the remaining 83% of the Ni comes from. One possibility is that it derives from the Ni content of diatom opal. However, given maximum diatom opal contents in these sediments of about 15% (Böning et al., 2004) and the Ni/Si ratio in diatom opal reported in Twining et al. (2012) of 28

μmol/mol, only a small fraction of the Ni in these sediments, again only a few %, can be associated with opal. Even a pure opal sediment would not get close to explaining the Ni inventory of the HF-digested fraction of the Peru sediments. Of course, it is well-established that only a fraction of the diatom opal produced in the photic zone survives transport through the water column (on average 10-15%; Tréguer et al., 1995), and that only a small portion of this survives dissolution within sediment (15-20%; Tréguer et al., 1995; Ragueneau et al., 2002). Thus if, in a manner analogous to that suggested above for the OPF, Ni is retained on residual opal while the silica is lost to the water column, then the delivery of diatom opal to these sediments can indeed explain the inventory we find in the HFD fraction.

The above discussion illustrates the necessity for further studies of water column particulate material if we are to better understand the pathways by which metals are delivered via export production from the photic zone to sediment, and if we are to robustly interpret data for ancient sediments. But, any process additional to those discussed above is required to preserve the strong relationship between sedimentary Ni contents and TOC. Though speculation at present, a potential process is the diffusion of Ni into sediment, driven by a concentration gradient in the dissolved phase as Ni is fixed into diagenetic solid phases beneath the sediment-water interface – in a process analogous to that thought to operate for uranium (e.g., Anderson, 1987; Andersen et al., 2014). In the succeeding section we use the isotope data to shed further light on these questions.

5.2. ***Nickel isotopes in the organic-pyrite fraction: a biogenic signal from the upper ocean***

The δ^{60}Ni data for the organic-pyrite fraction (Fig. 4b) is mostly in the range +0.86 to +1.39. As highlighted in Figures 6 and 7, the variability within this range comes with systematic relationships that suggest more specific links to water column processes. For example, most of the Peru Margin data in Figure 6 lie on an array that is consistent with Ni removal from a relatively homogeneous reservoir with a small isotope fractiona-

tion (-0.3 ‰, $\alpha = 0.9997$). These findings are consistent with the suggestion that the Ni in the OPF was taken up in the photic zone and that this signal has survived into the sediment relatively unmodified. For example, published data for the photic zone imply a fractionation factor associated with drawdown of 0.9997, and that upwelled deep water is about 0.3 - 0.4 ‰ heavier than the value at the lower end of the array on Figure 6 (Archer et al., 2017; Takano et al., 2017). Thus, many of the OPF data show systematics that are consistent with the hypothesis that this fraction represents a reservoir of Ni that is relatively unmodified after uptake into cells in the photic zone. Data for the core from below the Peru OMZ, as well as data for Lagoa Salgada also form an array on Figure 6, but with a much lower slope, possibly related to a different microbial ecology.

The scatter on Figure 6 might be due to post-uptake processes, the harsh treatment in the laboratory, but could also be due to biological processes. For example, two analyses from core MC6A lie at very high δ^{60}Ni, and are above the array on Figure 6. As shown in Figure 7, this variability in Ni isotopes may come with correlated variability in δ^{13}C – as do other aspects of the Ni isotope data from Peru and Lagoa Salgada. We cannot speculate here on the specific meaning of these relationships but their existence provides additional support for the suggestion that the Ni in the OPF, though there may be transfer to sulphide grains *within* the OPF package, derives from the site of biomass production, in this case probably the photic zone.

5.3. ***Detrital correction to bulk sediment and authigenic Ni in Peru Margin sediments***

It is well established that the organic-rich sediments of the Peru Margin are enriched in authigenic Ni (e.g., Böning et al., 2015). In order to establish the precise amount and isotopic composition of that authigenic Ni in the bulk analysis a correction for the detrital Ni inventory must be made. The conventional approach to such corrections is to use the concentration of Al or Ti as tracers of detrital input, as these elements are abundant in silicate minerals and present at low abundance in seawater (e.g., Brumsack, 1989). Thus:

$$[Ni]_{\text{authigenic}} = [Ni]_{\text{bulk sample}} - [Al]_{\text{bulk sample}} * (Ni/Al)_{\text{detrital}} \quad (3)$$

Böning et al. (2012) use the intercept on a plot of Ni/Al ratio versus TOC to define the Ni/Al ratio of the detrital fraction. The Ni/Al versus TOC data presented here (Fig. 5b) fall on arrays defining intercepts that range from slightly negative up to those found by Böning et al. (2012) for Peru OMZ samples. Here we apply the full range suggested by Böning et al. (2012) for upwelling regions, of 0-3.3*10^{-4} g/g, and propagate the uncertainty this range represents through to the final authigenic δ^{60}Ni.

Then the isotopic composition of the authigenic fraction is obtained from:

$$\delta^{60}Ni_{\text{authigenic}} = \frac{\delta^{60}Ni_{\text{bulk}} - f_{\text{detrital}}\delta^{60}Ni_{\text{detrital}}}{f_{\text{authigenic}}} \quad (4)$$

where $f_{\text{authigenic}}$ and f_{detrital} are the fractions of authigenic and detrital Ni in the sample, respectively, and $\delta^{60}Ni_{\text{bulk}}$, $\delta^{60}Ni_{\text{detrital}}$, and $\delta^{60}Ni_{\text{authigenic}}$ are the un-corrected bulk, detrital, and authigenic Ni isotope compositions, respectively. A value for $\delta^{60}Ni_{\text{detrital}}$ is required to derive the authigenic Ni isotope composition, and is conventionally taken to be that of the upper continental crust (UCC). Data for loess, river sediments, and basalts (n=15, Cameron et al., 2009) suggest a value of $+0.14 \pm 0.23$, which we use here. In Figure 8 the lower end of the vertical line for each sample represents no correction ($Ni/Al_{\text{detrital}} = 0$) while the upper end represents a $Ni/Al_{\text{detrital}} = 3.3$ and the lowest possible $\delta^{60}Ni_{\text{detrital}}$ given the data above, and thus the maximum possible corrected $\delta^{60}Ni_{\text{authigenic}}$. The Lagoa Salgada sediments are dominated by carbonate and their δ^{60}Ni are close to the UCC. The Ni/Al ratios of these sediments are also consistent with a lithogenic origin.

It is apparent from Figure 8 that the bulk $\delta^{60}Ni_{\text{authigenic}}$ obtained in this way, given the uncertainty in the correction introduced by that in the detrital Ni/Al ratio, are all

consistent with derivation from the water column dissolved pool. For un-corrected bulk Ni/Al ratios below about $1*10^{-3}$ g/g, and for the conservative range of detrital Ni/Al ratios used here, the correction is potentially very large, the resultant $\delta^{60}Ni_{authigenic}$ very uncertain, and it seems clear that the maximum $Ni/Al_{detrital}$ ratio assumed here over-corrects for detrital Ni. For Ni/Al ratios $>1*10^{-3}$ g/g the correction for detrital Ni is much smaller and $\delta^{60}Ni_{authigenic}$ is much more precisely known. It is also significant that, though recent data for the photic zone extend well above the deep ocean δ^{60}Ni to +1.7‰ (Archer et al., 2017; Takano et al., 2017), none of the more robust $\delta^{60}Ni_{authigenic}$ extend above about +1.3‰.

The suggestion that Ni in the HFD is not derived from the photic zone provides tentative support for the idea of inward diffusion from bottom water. Whatever the precise mechanism, it is clear that authigenic Ni in these sediments is derived from the water column with very little isotopic modification. This conclusion is very robust for sediments with bulk Ni/Al ratios $>1*10^{-3}$ g/g, and is also likely to be the case for sediments with Ni/Al ratios beneath this cutoff.

5.4. ***Re-assessment of the oceanic mass balance of Ni and its isotopes***

As outlined in the introduction, the Ni elemental and isotope budget of the ocean is apparently out of balance given our knowledge of the inputs and outputs (Cameron and Vance, 2014). We revisit this imbalance problem in the light of the new data presented here for a major sink of Ni from the oceans. The key parameters for this discussion are given in Table 2.

For the main input fluxes discussed in Cameron and Vance (2014) there is little new to add here. The dissolved load of rivers is a well-known input, and what is known about Ni behavior in the estuaries of large rivers does not suggest much deviation from conservative behavior (e.g., Boyle et al., 1982; Edmond et al., 1985). There is no evidence for a significant hydrothermal flux of Ni to the oceans. Indeed, recent GEOTRACES

sections (see Supplementary Information) suggest that hydrothermal plumes may be sites of Ni removal by scavenging. The maximum Ni concentrations that have been reported for hydrothermal fluids are from ultramafic substrates and reach 3 μM (Douville et al., 2002). Even if all hydrothermal fluids had this high concentration, and if none of the Ni in those fluids was removed close to the ridge by scavenging, this would imply a maximum hydrothermal Ni flux of order $9*10^7$ mol/yr. This is about 25% of the modern riverine flux of Ni, and must be a very substantial overestimate. Wheat et al. (2002) also calculate the flux of Ni from a warm ridge-flank hydrothermal system to be insignificant. In terms of outputs, Vance et al. (2016) and the current study provide new data documenting the output of Ni and its isotopes to anoxic and sulphidic sediments that have not yet been considered in the oceanic mass balance. We can estimate the sizes of these two sinks given the Ni/TOC ratio of the sediments and published estimates for the organic carbon burial fluxes in these settings (e.g., Hedges and Keil, 1995), as is done in Table 2. Given the Ni/TOC ratio of Lagoa Salgada sediments of $1.4*10^{-4}$, and a global carbon burial flux associated with carbonate sediments of $6*10^{12}$ g/yr, we also estimate a Ni burial flux to carbonate sediments of $1.4*10^7$ mol/yr.

As discussed in Gall et al. (2013) and Cameron and Vance (2014), the final major output of Ni from the oceans is likely to be sorption to and burial of particulate Fe-Mn oxides. The size of this output has variously been estimated at $1.5*10^9$ mol/yr (Cameron and Vance, 2014) to $5.1*10^8$ mol/yr (Gall et al., 2013). These estimates, however, present a mass balance problem in that the size of the total quantified output they imply, taken together with the data presented here, is 2-5 times the quantified input. At face value, the above elemental imbalance suggests that there must be a large and as yet unquantified input flux. One possibility is that the dissolved phase of rivers does not represent the entire input to the oceans from this source, and that there is significant mobilization of Ni from the particulate load, as has been suggested for other elements (e.g., Oelkers et al., 2012). A second possibility is that the large and poorly-constrained Fe-Mn output flux is much smaller than the above estimates imply.

The isotopic characteristics of the various inputs and outputs have an important bearing on this mass balance problem. In general, the issue with the isotope mass balance is that all the known inputs have an isotope composition that is lighter than seawater, while the largest known outputs are either heavier than seawater (Gall et al., 2013) or very close to it (this study). Isotope data appears to rule out potential issues with uncertainties in the immediately obvious additional inputs. For example, though the labile portion of riverine particulates can provide the missing input, early data for the isotope composition of Ni in these phases suggests that it is no different from the upper continental crust (Revels et al., 2017), and thus also lighter than seawater. A much bigger dust input than previously imagined would have the same problem. As discussed earlier, the hydrothermal flux of Ni to the oceans is almost certainly insignificant and, given the homogeneity of the Ni isotope composition of the basalts from which they derive (Cameron et al., 2009; Elliott and Steele, 2017), it would also come with the same problem.

We suggest that the solution to these budget problems may lie with diagenetic processes that are likely to occur under both oxic and suboxic conditions, processes that may drive an as yet un-quantified flux of Ni back out of sediments. Atkins et al. (2016) have suggested that an additional benthic input to the ocean could result from the release of Ni (up to about 50%) to the water column upon transformation of birnessite to todorokite in oxic settings. If such a back-flux were isotopically heavy this could solve both the elemental and isotopic imbalances. Such a solution would, however, require that all the Fe-Mn crusts measured thus far have not undergone this birnessite-todorokite transition and that there must exist some Fe-Mn deposits that represent the final buried output from the dissolved pool and that are not yet characterized. Shaw et al. (1990) present pore water data that mobilization of Ni into pore water (with concentrations as high as 600 nM) that is clearly coupled to the reductive dissolution of dispersed Mn-oxide coatings in reducing sediments. In situations where the redox conditions at the sediment-water interface remain in the Mn-reducing regime, Ni could leak back out of sediment and into

the water column.

Figure 9 investigates what is required, in terms of flux and isotope composition, of some of these less well constrained aspects of the budget. The black curve in Figure 9 shows the required size and isotopic composition of a putative missing input given a possible range in the size of the *buried* Fe-Mn oxide output (e.g., after a diagenetic back-flux from sediment to the water column has occurred), from that required to balance the currently known inputs (missing input = zero) up to the value of $1.5*10^9$ mol/yr estimated by Cameron and Vance (2014). For all possible sizes of such an extra input, its isotope composition would have to be heavier than any known terrestrial δ^{60}Ni. Alternatively, the red curve sets the δ^{60}Ni of the missing input to the value of the UCC (e.g., the Ni that is potentially released from riverine particulates) and considers how the isotope budget could be balanced if the buried Fe-Mn oxide output (e.g. again after diagenetic modification) could have a different δ^{60}Ni from that measured for Fe-Mn crusts. Clearly, this latter option would require that heavy Ni is lost back to the ocean during re-mobilization of Ni from Fe-Mn oxides.

6. Conclusions

The twin objectives of this study were: (1) to understand and quantify an important sedimentary sink for Ni isotopes, that into Ni-enriched sediments in productive upwelling settings, and; (2) to investigate the degree to which a water column Ni isotope signature can be extracted from sediments – both from the bulk sediment inventory and through the isolation of different fractions. We find that an organic and sulphide rich residue (an organic plus pyrite fraction – OPF), isolated from both organic-rich and carbonate sediments after HF digestion, preserves δ^{60}Ni that is close to the modern water column, at $+1.3 \pm 0.4$ ‰. The detailed Ni-TOC-δ^{60}Ni-δ^{13}C characteristics of this fraction record processes occurring at the site of biomass production and Ni uptake (e.g., photic zone), and appears to remain a pseudo-closed system for Ni and its isotopes during transfer through the water column and delivery to the sediment-water interface. For bulk samples from up-

525 welling zones that are highly enriched in Ni (Ni/Al $> 10^{-3}$ g/g), and where correction for
526 detrital Ni input is not significant, the HF-digestible fraction, which dominates the non-
527 detrital fraction of the bulk sediment, records the average δ^{60}Ni of the modern deep ocean.
528
529 Although the upwelling margin sediments investigated here are an important sink for
530 Ni from the ocean, their δ^{60}Ni is so close to that of modern seawater that they exert very
531 little isotopic leverage on the water column, and the heavy isotope composition of modern
532 water column Ni must have other drivers. The methodological approach presented here,
533 involving the isolation and analysis of different fractions of the bulk sediment, has the
534 potential to provide records of this water column isotope composition back through time,
535 as well as to quantify isotope fractionations associated with biological uptake in the past,
536 for Ni and perhaps for other transition metals too.

537 **Acknowledgments**

538 We wish to thank T. Eglinton, C. Vasconcelos, and C. Bovier for providing samples.
539 For help and support in the lab we greatly thank C. Archer, and M.Jaggi. We thank Shui-
540 Jiong Wang and an anonymous reviewer for their constructive comments on an earlier
541 version of this paper, and Louis Derry for editorial handling. This research was funded
542 by the Swiss National Science Fund (grants 200021_143262 and 200020_165904) and ETH
543 Zürich.

544 **References**

545 Andersen, M. B., Romaniello, S., Vance, D., Little, S. H., Herdman, R., Lyons, T. W.,
546 2014. A modern framework for the interpretation of ^{238}U/^{235}U in studies of ancient
547 ocean redox. Earth and Planetary Science Letters 400, 184–194.

548 Anderson, R. F., 1987. Redox behavior of uranium in an anoxic marine basin. Uranium
549 3, 145–164.

550 Archer, C., Vance, D., Lohan, M. C., 2017. Negligible Ni Isotope Fractionation Associated
551 with Phytoplankton Uptake in the South Atlantic Ocean. Goldschmidt Abstarcts, 131.
552 URL https://goldschmidtabstracts.info/2017/131.pdf

553 Arnold, G. L., Anbar, A. D., Barling, J., Lyons, T. W., 2004. Molybdenum Isotope
554 Evidence for Widespread Anoxia in Mid-Proterozoic Oceans. Science 304, 87–90.

555 Atkins, A. L., Shaw, S., Peacock, C. L., 2016. Release of Ni from birnessite during trans-
556 formation of birnessite to todorokite: Implications for Ni cycling in marine sediments.
557 Geochimica et Cosmochimica Acta 189, 158–183.

558 Birgel, D., Meister, P., Lundberg, R., Horath, T. D., Bontognali, T. R. R., Bahniuk,
559 A. M., de Rezende, C. E., Vasconcelos, C., McKenzie, J. A., 2015. Methanogenesis
560 produces strong ^{13}C enrichment in stromatolites of Lagoa Salgada, Brazil: a modern
561 analogue for Palaeo-Neoproterozoic stromatolites? Geobiology 13, 245–266.

562 Böning, P., Brumsack, H.-J., Böttcher, M. E., Schnetger, B., Kriete, C., Kallmeyer, J.,
563 Borchers, S. L., 2004. Geochemistry of Peruvian near-surface sediments. Geochimica et
564 Cosmochimica Acta 68, 4429–4451.

565 Böning, P., Fröllje, H., Beck, M., Schnetger, B., Brumsack, H.-J., 2012. Underestimation
566 of the authigenic fraction of Cu and Ni in organic-rich sediments. Marine Geology 323-
567 325, 24–28.

568 Böning, P., Shaw, T., Pahnke, K., Brumsack, H.-J., 2015. Nickel as indicator of fresh
569 organic matter in upwelling sediments. Geochimica et Cosmochimica Acta 162, 99–108.

570 Bovier, C., 2015. Sedimentological and geochemical studies on microbialite structures and
571 sediments from Lagoa Salgada, Rio de Janeiro, Brazil. Master Thesis ETH Z?rich.

572 Boyle, E. A., Huested, S. S., Grant, B., 1982. The chemical mass balance of the amazon
573 plume?II. Copper, nickel, and cadmium. Deep Sea Research Part A. Oceanographic
574 Research Papers 29, 1355–1364.

575 Bruland, K. W., 1980. Oceanographic distributions of cadmium, zinc, nickel, and copper
576 in the North Pacific. Earth and Planetary Science Letters 47, 176–198.

577 Bruland, K. W., Lohan, M. C., 2003. Controls of trace metals in seawater. Treaties on
578 Geochemistry 6, 23–47.

579 Brumsack, H. J., 1989. Geochemistry of recent TOC-rich sediments from the Gulf of
580 California and the Black Sea. Geologische Rundschau 78, 851–882.

581 Calvert, S. E., Price, N. B., 1983. Geochemistry of Namibian shelf sediments. In: Coastal
582 Upwelling Its Sediment Record. Springer, pp. 337–375.

583 Cameron, V., Vance, D., 2014. Heavy nickel isotope compositions in rivers and the oceans.
584 Geochimica et Cosmochimica Acta 128, 195–211.

585 Cameron, V., Vance, D., Archer, C., House, C. H., 2009. A biomarker based on the stable
586 isotopes of nickel. Proceedings of the National Academy of Sciences 106, 10944–10948.

587 Desboeufs, K., Sofikitis, A., Losno, R., Colin, J., Ausset, P., 2005. Dissolution and solubil-
588 ity of trace metals from natural and anthropogenic aerosol particulate matter. Chemo-
589 sphere 58, 195–203.

590 Douville, E., Charlou, J. L., Oelkers, E. H., Bienvenu, P., Jove Colon, C. F., Donval,
591 J. P., Fouquet, Y., Prieur, D., Appriou, P., 2002. The rainbow vent fluids (36°14'N,
592 MAR): the influence of ultramafic rocks and phase separation on trace metal content
593 in Mid-Atlantic Ridge hydrothermal fluids. Chemical Geology 184, 37–48.

594 Edmond, J. M., Spivack, A., Grant, B. C., Ming-Hui, H., Zexiam; Chen Sung;
595 Zeng Xiushau, C., 1985. Chemical dynamics of the Changjiang estuary. Continental
596 Shelf Research 4, 17–36.

597 Eigenbrode, J. L., Freeman, K. H., Oct. 2006. Late Archean rise of aerobic microbial
598 ecosystems. Proceedings of the National Academy of Sciences 103, 15759–15764.

599 Elliott, T., Steele, R. C. J., 2017. The Isotope Geochemistry of Ni. Reviews in Mineralogy
600 and Geochemistry 82, 511–542.

601 Fuenzalida, R., Schneider, W., Garcés-Vargas, J., Bravo, L., Lange, C., 2009. Vertical and
602 horizontal extension of the oxygen minimum zone in the eastern South Pacific Ocean.
603 Deep Sea Research Part II: Topical Studies in Oceanography 56, 992–1003.

604 Fujii, T., Moynier, F., Blichert-Toft, J., Albaréde, F., 2014. Density functional theory
605 estimation of isotope fractionation of Fe, Ni, Cu, and Zn among species relevant to
606 geochemical and biological environments. Geochimica et Cosmochimica Acta 140, 553–
607 576.

608 Gall, L., Williams, H., Siebert, C., Halliday, A., Herrington, R., Hein, J., 2013. Nickel
609 isotopic compositions of ferromanganese crusts and the constancy of deep ocean inputs
610 and continental weathering effects over the Cenozoic. Earth and Planetary Science
611 Letters 375, 148–155.

612 Gueguen, B., Rouxel, O., Ponzevera, E., Bekker, A., Fouquet, Y., 2013. Nickel Isotope
613 Variations in Terrestrial Silicate Rocks and Geological Reference Materials Measured
614 by MC-ICP-MS. Geostand Geoanal Res 37, 297–317.

615 Gueguen, B., Rouxel, O., Rouget, M.-L., Bollinger, C., Ponzevera, E., Germain, Y., Fou-
616 quet, Y., Sep. 2016. Comparative geochemistry of four ferromanganese crusts from the
617 Pacific Ocean and significance for the use of Ni isotopes as paleoceanographic tracers.
618 Geochimica et Cosmochimica Acta 189, 214–235.

619 Hedges, J. I., Keil, R. G., 1995. Sedimentary organic matter preservation: an assessment
620 and speculative synthesis. Marine Chemistry 49, 81–115.

621 Ingall, E., Jahnke, R., Jun. 1994. Evidence for enhanced phosphorus regeneration from
622 marine sediments overlain by oxygen depleted waters. Geochimica et Cosmochimica
623 Acta 58, 2571–2575.

624 Janssen, D. J., Conway, T. M., John, S. G., Christian, J. R., Kramer, D. I., Pedersen,
625 T. F., Cullen, J. T., 2014. Undocumented water column sink for cadmium in open ocean
626 oxygen-deficient zones. PNAS 111, 6888–6893.

627 Janssen, D. J., Cullen, J. T., 2015. Decoupling of zinc and silicic acid in the subarctic
628 northeast Pacific interior. Marine Chemistry 177, 124–133.

629 Jickells, T. D., An, Z. S., Andersen, K. K., Baker, A. R., Bergametti, G., Brooks, N., Cao,
630 J. J., Boyd, P. W., Duce, R. A., Hunter, K. A., Kawahata, H., Kubilay, N., laRoche, J.,
631 Liss, P. S., Mahowald, N., Prospero, J. M., Ridgwell, A. J., Tegen, I., Torres, R., 2005.
632 Global Iron Connections Between Desert Dust, Ocean Biogeochemistry, and Climate.
633 Science 308, 67–71.

634 Kasting, J., 2005. Methane and climate during the Precambrian era. Precambrian Re-
635 search 137, 119–129.

636 Konhauser, K. O., Pecoits, E., Lalonde, S. V., Papineau, D., Nisbet, E. G., Barley,
637 M. E., Arndt, N. T., Zahnle, K., Kamber, B. S., 2009. Oceanic nickel depletion and a
638 methanogen famine before the Great Oxidation Event. Nature 458, nature07858.

639 Lai, X., Norisuye, K., Mikata, M., Minami, T., Bowie, A. R., Sohrin, Y., 2008. Spatial
640 and temporal distribution of Fe, Ni, Cu and Pb along 140°E in the Southern Ocean
641 during austral summer 2001/02. Marine Chemistry 111, 171–183.

642 Landing, W. M., Lewis, B. L., 1991. Thermodynamic Modeling of Trace Metal Speciation
643 in the Black Sea. In: Black Sea Oceanography. NATO ASI Series. Springer, Dordrecht,
644 pp. 125–160.

645 Little, S., Vance, D., Walker-Brown, C., Landing, W., 2014. The oceanic mass balance
646 of copper and zinc isotopes, investigated by analysis of their inputs, and outputs to
647 ferromanganese oxide sediments. Geochimica et Cosmochimica Acta 125, 673–693.

Little, S. H., Vance, D., Lyons, T. W., McManus, J., 2015. Controls on trace metal authigenic enrichment in reducing sediments: Insights from modern oxygen-deficient settings. American Journal of Science 315, 77–119.

Mackey, D. J., O'Sullivan, J. E., Watson, R. J., Dal Pont, G., 2002. Trace metals in the Western Pacific: temporal and spatial variability in the concentrations of Cd, Cu, Mn and Ni. Deep Sea Research Part I: Oceanographic Research Papers 49, 2241–2259.

Oelkers, E. H., Jones, M. T., Pearce, C. R., Jeandel, C., Eiriksdottir, E. S., Gislason, S. R., 2012. Riverine particulate material dissolution in seawater and its implications for the global cycles of the elements. Comptes Rendus Geoscience 344, 646–651.

Ohnemus, D. C., Rauschenberg, S., Cutter, G. A., Fitzsimmons, J. N., Sherrell, R. M., Twining, B. S., 2016. Elevated trace metal content of prokaryotic communities associated with marine oxygen deficient zones. Limnology and Oceanography 62, 3–25.

Paytan, A., McLaughlin, K., Feb. 2007. The Oceanic Phosphorus Cycle. Chem. Rev. 107, 563–576.

Peacock, C. L., Sherman, D. M., 2007. Sorption of Ni by birnessite: Equilibrium controls on Ni in seawater. Chemical Geology 238, 94–106.

Pons, M.-L., Fujii, T., Rosing, M., Quitté, G., Télouk, P., Albaréde, F., 2013. A Zn isotope perspective on the rise of continents. Geobiology 11, 201–214.

Ragsdale, S. W., 2009. Nickel-based Enzyme Systems. Journal of Biological Chemistry 284, 18571–18575.

Ragueneau, O., Dittert, N., Pondaven, P., Tréguer, P., Corrin, L., 2002. Si/C decoupling in the world ocean: is the Southern Ocean different? Deep Sea Research Part II: Topical Studies in Oceanography 49, 3127–3154.

Revels, B., Rickli, J., Moura, C., Vance, D., 2017. Phase Partitioning of Transition Metals and their Isotopes in the Particulate Load of the Amazon River. Goldschmidt Abstracts,

673 3328.
674 URL https://goldschmidtabstracts.info/2017/3328.pdf

675 Rudnick, R., Gao, S., 2014. Composition of the Continental Crust. In: Treatise on Geo-
676 chemistry. Elsevier, pp. 1–51.

677 Sclater, F. R., Boyle, E., Edmond, J. M., 1976. On the marine geochemistry of nickel.
678 Earth and Planetary Science Letters 31, 119–128.

679 Shaw, T. J., Gieskes, J. M., Jahnke, R. A., 1990. Early diagenesis in differing deposi-
680 tional environments: The response of transition metals in pore water. Geochimica et
681 Cosmochimica Acta 54, 1233–1246.

682 Siebert, C., Nägler, T. F., von Blanckenburg, F., Kramers, J. D., 2003. Molybdenum
683 isotope records as a potential new proxy for paleoceanography. Earth and Planetary
684 Science Letters 211, 159–171.

685 Suess, E., Kulm, L. D., Killingley, J. S., 1987. Coastal upwelling and a history of organic-
686 rich mudstone deposition off Peru. Geological Society, London, Special Publications 26,
687 181–197.

688 Takano, S., Tanimizu, M., Hirata, T., Shin, K.-C., Fukami, Y., Suzuki, K., Sohrin, Y.,
689 2017. A simple and rapid method for isotopic analysis of nickel, copper, and zinc in
690 seawater using chelating extraction and anion exchange. Analytica Chimica Acta 967,
691 1–11.

692 Tréguer, P., Nelson, D. M., Van Bennekom, A. J., Demaster, D. J., Leynaert, A.,
693 Quéguiner, B., 1995. The silica balance in the world ocean: a reestimate. Science 268,
694 375–379.

695 Twining, B. S., Baines, S. B., Bozard, J. B., Vogt, S., Walker, E. A., Nelson, D. M., 2011.
696 Metal quotas of plankton in the equatorial Pacific Ocean. Deep Sea Research Part II:
697 Topical Studies in Oceanography 58, 325–341.

Twining, B. S., Baines, S. B., Vogt, S., Nelson, D. M., Dec. 2012. Role of diatoms in nickel biogeochemistry in the ocean. Global Biogeochemical Cycles 26, GB4001.

Vance, D., Little, S. H., Archer, C., Cameron, V., Andersen, M. B., Rijkenberg, M. J. A., Lyons, T. W., 2016. The oceanic budgets of nickel and zinc isotopes: the importance of sulfidic environments as illustrated by the Black Sea. Philosophical Transactions of the Royal Society A: Mathematical, Physical and Engineering Sciences 374, 20150294.

Wheat, C. G., Mottl, M. J., Rudnicki, M., 2002. Trace element and REE composition of a low-temperature ridge-flank hydrothermal spring. Geochimica et Cosmochimica Acta 66, 3693–3705.

Figure captions

Fig.1: Published Ni isotope data for seawater compared to that of the discharge weighted average for the dissolved phase of rivers (turquoise line) and to that of the upper continental crust (UCC, brown line). Data from Cameron and Vance (2014) and Takano et al. (2017).

Fig.2: Map of sample provenance (a). Details of the Peru margin setting (b) where core-top samples (black diamonds) and three down-core profiles (colorful symbols) were taken. Grey shading indicates bathymetry whereas colors indicate bottom water oxygen. Oxygen data from CTD casts was gridded in ODV with DIVA scaling. Details of the Lagoa Salgada setting(c) modified from Birgel et al. (2015).

Fig.3: TOC data for the bulk samples, measured before any HF-HCl treatment, plotted versus the TOC content of the OPF, obtained after the HF-HCl digestion. Plotted error bars reflect the repeatability of standards and samples and are ±15% (relative). Most data fall on an array (solid line, slope = 0.9) that implies 90% retention of the organic carbon in the OPF after the HF digestion. The dashed lines bracket nearly all the data

and have slopes of 0.6 and 1.2.

Fig.4: Peru margin Ni abundances and isotope composition calculated for bulk samples (a) and as measured for the respective OPF and HFD fractions of the same samples (b). The blue line and associated band indicate the average and 2σ of the Ni isotopic composition of the modern deep ocean (defined by depths greater than 1000m, references in text).

Fig.5: Ni abundances plotted versus TOC for the sediments studied here. (a) Data for Peru Margin bulk sediments, compared to data reported in Böning et al. (2015) for sediments in upwelling regions globally. The strong correlation between Ni abundance and TOC in the OMZ sediments suggests delivery of Ni to the sediments via organic matter (data in gray from Böning et al., 2015). (b) Ni/Al vs. TOC for the Peru Margin sediments studied here. The Ni organic matter association for Peru margin samples is further supported by (c) the correlation between Ni abundance in the OPF fraction versus %orgC in the OPF and (d) the strong correlation between Ni and P abundances in the OPF fraction in all but two of the Peru Margin samples.

Fig.6: δ^{60}Ni vs. ln[Ni] in the organic-pyrite fractions (OPF) of Peru Margin and Lagoa Salgada sediments. Most Peru Margin samples for cores within the OMZ, as well as all core-top samples, lie on an array that is consistent with removal of Ni from a water column with a Ni isotopic composition close to the deep ocean value. The arrow labeled $\alpha = 0.9997$ shows the expected array if the Ni in the OPF is derived from the photic zone with preferential removal of the light isotope as observed in the water column (Archer et al., 2017; Takano et al., 2017). Most of the data for the Peru Margin samples are consistent with this process. Data for both the Peru Margin core from beneath the OMZ and the Lagoa Salgada may define a fractionation trend representing an alpha that is closer to 1.

Fig.7: δ^{60}Ni vs. δ^{13}C. Peru margin down-core sediments from the upper edge of and below the OMZ show inverse correlations between δ^{60}Ni and δ^{13}C of the OPF fraction that appear to be specific to each location. (b) Lagoa Salgada OPF fractions exhibit an opposite (positive) correlation between δ^{60}Ni and δ^{13}C.

Fig.8: Peru Margin authigenic δ^{60}Ni obtained after a correction for detrital Ni, using Ni/Al detrital of 0 (i.e., no correction, filled symbols) and of $3.3*10^{-4}$ g/g (empty symbols). The bars between the empty and filled symbol of each sample indicate the range along which the $\delta^{60}Ni_{authigenic}$ could lie. The blue line and associated band indicate the average and 2σ of the Ni isotopic composition of the modern deep ocean (defined by depths greater than 1000m, references in text).

Fig.9: Requirements of two alternative ways to balance the oceanic budget of Ni and its isotopes. The black curve shows the required isotope composition of a projected missing input versus its size, given a range in size of the Fe-Mn oxide output from that required to balance the currently known inputs (missing input = zero) up to $1.5*10^9$ mol/yr (Cameron and Vance, 2014). The δ^{60}Ni of the Fe-Mn oxide output is taken to be the average of data in Gall et al. (2013). The red curve assumes that the required missing input has an isotope composition the same as the upper continental crust, and explores the δ^{60}Ni of the effective – e.g. final buried - Fe-Mn oxide output following potential diagenetic modification. Other parameters, for the size and isotopic composition of the better known inputs and outputs, as summarized in Table 3.

Table 1: Elemental and isotope data for Peru Margin and Lagoa Salgada sediments.

sample	water depth or depth in core[1] (m) or (cm)	BWO[1] (μM)	OPF wt%[2]	OPF C (wt%)	OPF δ^{13}C (‰)	OPF Ni (ppm)[3]	OPF Ni (% of tot)	OPF Al (wt %)	OPF P (ppm)	OPF δ^{60}Ni (‰)	OPF 2σ[4]	HFD Ni (ppm)	HFD Ni (% of tot)	HFD Al (wt%)	HFD δ^{60}Ni (‰)	HFD 2σ	Bulk[6] TOC[1] (wt%)	Bulk[6] δ^{13}C (‰)	Bulk[6] Ni (ppm)	Bulk[6] Al (wt%)	Bulk[6] Ni/Al[5]	Bulk[6] δ^{60}Ni (‰)	Bulk[6] 2σ
R/V Seward Johnson 10-92, core-tops																							
BC39	550	10	20	3.4	-20.9	9.8	14	1.0	325	1.24	0.10	61	86	2.3	1.06	0.08	3.4	-21.1	70	3.3	21	1.09	0.08
BC57	172	<10	34	12	-20.8	13	15	0.7	99	1.02	0.08	76	85	4.1	1.07	0.08	9.6	-20.5	89	1.8	21	1.06	0.08
BC62	643	10	21	4.4	-21.3	7.5	17	0.9	34	1.08	0.05	38	83	5.2	1.26	0.05	5.0	-20.9	45	6.1	7.4	1.23	0.05
BC76	725	15	30	4.9	-21.2	8.5	17	1.5	48	1.15	0.10	42	83	4.8	1.37	0.07	6.6	-21.1	50	6.2	8	1.33	0.08
BC81	130	10	36	11	-20.7	17	21	1.1	71	1.15	0.06	62	79	4.5	1.08	0.08	10.6	n/a	79	5.6	14	1.09	0.07
KC83	106	10	44	7.9	-20.4	12	24	1.3	71	1.14	0.07	37	76	3.0	1.04	0.05	7.8	-20.2	49	4.4	11	1.07	0.06
BC93	100	5	25	3.4	-20.8	5.6	16	0.3	20	1.30	0.08	29	84	5.1	1.05	0.06	3.7	-20.5	35	5.4	6.5	1.09	0.06
BC125	340	5	36	7.6	-21.3	10	13	0.7	94	0.91	0.10	65	87	4.7	1.20	0.07	8.1	-20.7	75	5.4	14	1.16	0.08
KC127	309	5	45	4.1	-20.9	16	18	0.4	57	1.04	0.07	70	82	2.6	1.17	0.07	9.9	-20.6	85	3.0	29	1.15	0.07
BC153	250	5	51	8.7	-20.9	9.4	11	0.1	29	0.98	0.09	75	89	2.5	1.14	0.06	9.7	-20.8	84	2.6	32	1.12	0.08
R/V Knorr 182-9, core MC6A, 100m water depth, upper OMZ																							
MC6A1	0-1	2.2	34	2.9	-21.2	7.8	20	0.7	21	1.28	0.07	30	80	2.6	1.04	0.08	5.4	n/a	38	3.3	13	1.09	0.07
MC6A6	5-6	2.2	36	4.0	-20.4	9.6	21	0.8	29	1.28	0.07	36	79	2.3	0.92	0.07	5.9	-20.7	46	3.2	16	0.99	0.07
MC6A14	13-14	2.2	32	3.7	-20.3	9.6	21	0.9	39	1.28	0.07	37	79	2.6	0.86	0.07	6.0	-20.7	47	3.4	15	0.94	0.07
MC6A16	15-16	2.2	30	3.4	-21.2	11	24	1.1	23	n/a	n/a	36	76	3.3	n/a	n/a	5.1	-21.2	47	4.4	11	n/a	n/a
MC6A22	21-22	2.2	22	2.2	-22.2	6.0	20	0.9	18	1.71	0.08	25	80	3.2	0.97	0.08	3.3	-22.2	31	4.1	8.4	1.11	0.08
MC6A26	25-26	2.2	24	2.9	-21.8	9.1	24	1.2	28	1.83	0.07	29	76	3.1	0.90	0.09	4.0	-21.8	38	4.2	10	1.12	0.09
MC6A37	36-37	2.2	19	3.2	-20.8	15	30	0.5	31	n/a	n/a	35	70	3.2	n/a	n/a	5.1	-20.9	50	3.7	13	n/a	n/a
MC6A4446	44-46	2.2	20	3.1	-20.9	7.5	20	0.8	15	1.40	0.08	30	80	3.0	0.89	0.06	3.7	n/a	37	3.9	11	0.99	0.07
R/V Knorr 182-9, core MC9G, 1500m water depth, below OMZ																							
MC9G1	0-1	80	19	1.0	-21.5	2.1	11	0.4	18	1.21	0.08	17	89	3.4	1.15	0.08	1.6	n/a	19	3.8	5.9	1.16	0.08
MC9G3	2-3	80	19	1.1	-21.4	2.7	13	0.4	31	n/a	n/a	18	87	3.5	n/a	n/a	2.2	-21.6	21	3.9	5.3	n/a	n/a
MC9G5	4-5	80	16	1.0	-21.1	2.2	12	0.4	17	n/a	n/a	17	88	3.7	n/a	n/a	2.0	-21.6	19	4.1	4.6	n/a	n/a
MC9G7	6-7	80	14	1.0	-20.9	0.8	4.2	0.2	6.6	1.13	0.09	18	96	4.0	1.12	0.05	1.8	-21.7	18	4.2	4.9	1.12	0.06
MC9G9	8-9	80	15	1.0	-21.2	1.4	7.3	0.4	8.5	n/a	n/a	18	93	3.8	n/a	n/a	2.3	-21.6	19	4.2	4.6	n/a	n/a
MC9G11	10-11	80	17	1.2	-20.5	2.7	12	0.3	8.4	0.96	0.09	19	88	3.7	1.15	0.06	1.6	n/a	22	4.0	6.0	1.12	0.06
MC9G13	12-13	80	14	1.2	-20.6	2.1	11	0.4	8.1	1.02	0.08	17	89	3.5	1.18	0.07	1.7	-21.8	19	3.9	5.5	1.16	0.07
R/V Knorr 182-9, core MC11C, 325m water depth, within OMZ																							
MC11C4	3-4	2.1	43	16	-21.2	25	18	0.7	139	0.96	0.08	112	82	1.7	1.20	0.09	14.2	-21.3	138	2.4	66	1.16	0.09
MC11C8	7-8	2.1	35	10	-21.8	22	17	0.7	123	0.94	0.05	104	83	1.8	1.20	0.09	12.9	-21.7	126	2.6	55	1.15	0.08
MC11C17	16-17	2.1	31	7.1	-22.0	22	19	0.9	128	0.98	0.06	95	81	2.2	1.27	0.12	11.8	-21.7	118	3.1	41	1.21	0.11
MC11C23	22-23	2.1	30	8.0	-21.9	23	20	0.8	133	n/a	n/a	95	80	2.1	n/a	n/a	11.5	-21.7	118	2.9	41	n/a	n/a
MC11C28	27-28	2.1	30	7.1	-21.8	22	17	0.7	98	0.86	0.06	106	83	2.6	1.17	0.07	12.0	-21.8	127	3.3	42	1.11	0.07
MC11C35	34-35	2.1	15	5.1	-22.0	16	20	0.3	86	0.93	0.06	66	80	2.2	1.22	0.06	10.3	n/a	82	2.5	36	1.16	0.06
MC11C37	36-37	2.1	29	6.6	-21.7	26	19	0.9	176	n/a	n/a	113	81	2.3	n/a	n/a	12.6	-21.4	139	3.2	44	n/a	n/a
MC11C4648	46-48	2.1	31	9.4	-21.6	26	20	1.0	334	n/a	n/a	102	80	1.7	n/a	n/a	10.8	-21.4	127	2.8	46	n/a	n/a
Lagoa Salgada																							
LS14	14.8-15.8	n/a	12	5.2	-11.3	0.31	13	0.04	8.5	1.58	0.05	2.0	87	0.80	0.41	0.15	7.4	n/a	2.3	0.84	2.7	0.46	0.14
LS20	20.8-21.8	n/a	10	1.8	-15.8	0.17	6.6	0.1	3.2	1.21	0.06	2.4	93	0.85	0.33	0.11	2.6	n/a	2.6	0.96	2.7	0.34	0.11
LS25	24.8-25.8	n/a	13	2.4	-10.8	0.19	10	0.2	5.1	1.28	0.06	1.8	90	0.77	0.13	0.05	3.2	n/a	2.0	0.93	2.1	0.21	0.05
LS30	29.8-30.8	n/a	9.1	0.9	-7.0	0.07	3.4	0.2	2.9	1.58	0.08	2.1	97	0.72	0.10	0.07	2.4	n/a	2.1	0.94	2.3	0.12	0.07
LS35	34.8-35.8	n/a	10	1.5	-7.6	0.24	6.7	0.4	4.8	1.31	0.08	3.3	93	0.91	-0.03	0.06	2.4	n/a	3.5	1.3	2.7	0.04	0.06
LS40	39.8-40.8	n/a	11	1.6	-9.0	0.21	6.3	0.4	5.6	1.34	0.05	3.0	94	0.80	0.04	0.07	2.1	n/a	3.3	1.2	2.7	0.10	0.07
LS45	44.8-45.8	n/a	6.0	1.3	-10.2	0.20	5.3	0.1	3.5	1.34	0.06	3.6	95	1.2	0.11	0.08	3.2	n/a	3.9	1.4	2.9	0.15	0.08
LS65	65.8-66.6	n/a	27	2.3	-23.5	0.71	4.8	1.1	1.2	1.10	0.04	14	95	1.3	n/a	n/a	3.4	n/a	15	2.4	6.1	n/a	n/a

[1]Water depth for R/V Seward Johnson samples and depth in core for all other samples; BWO is bottom water oxygen: TOC measured in bulk sample. [2]wt% of total sample found to be in the OPF. [3]Nickel concentrations obtained from the Element analysis. Nickel concentrations obtained by Element analysis and isotope dilution agree to within 10 - 20 %, but Element concentrations are used in all diagrams because of the importance of Ni/Al ratios to the interpretation. [4]The 2σ uncertainties reported here are internal errors propagated through the double spike reduction procedure. [5]All Ni/Al ratios are to be $*10^{-4}$. [6]Data for the 'Bulk' are calculated as the sum of the OPF and HFD fractions.

Table 2: Ni amounts, fluxes, and isotope compositions relevant to the modern oceanic mass balance.

Reservoir	Mass flux	Ref*	Ni concentration		Ref*	Ni flux (mol/yr)		Ref*	δ^{60}Ni (‰)		Ref*
			range	best estimate		range	best estimate		range	best estimate	
Global oceans			2.0-12 nM	8.0 nM	1				1.20-1.74	1.39	2-3
Input fluxes											
Rivers			2.5-35 nM	9.6 nM	2		$3.6*10^8$	2		0.80	2
Dust	$4.50*10^{11}$ kg/yr	4	36-58 ppm	47 ppm	5	$2.7\text{-}4.5*10^8$	$3.6*10^8$		-0.09-0.37	0.14	7
							2.1 % solubility	6			
						$5.8\text{-}9.4*10^6$	$7.6*10^6$				
Total							$3.7*10^8$			0.79	
Output fluxes											
Fe-Mn crusts							$1.5*10^9$	2			
							$5.1*10^8$	8	0.9-2.5	1.6	8
Euxinic seds	$1.0*10^{12}$ gC_{org}/yr	9	21-70 ppm	46 ppm	10						
			$0.54\text{-}1.49*10^{-3}$ Ni/TOC	9.0*10−4 Ni/TOC	10,11	$9.3\text{-}25*10^7$	$1.5*10^7$	this study	0.3-0.6	0.45	10
OMZ seds	$1.0*10^{13}$ gC_{org}/yr	9	21-158 ppm	69 ppm	this study						
			$0.63\text{-}1.56*10^{-3}$ Ni/TOC	$9.5*10^{-4}$ Ni/TOC	this study	$1.1\text{-}2.7*10^8$	$1.6*10^8$	this study	1.19-1.20	1.22	this study[1]
Carbonates	$6.0*10^{12}$ gC_{org}/yr	9	2.2-3.9 ppm	3.1 ppm	this study						
			$0.30\text{-}4.30*10^{-4}$ Ni/TOC	$1.4*10^{-4}$ Ni/TOC	this study	$0.31\text{-}4.4*10^7$	$1.4*10^7$	this study	1.10-1.64	1.29	this study[2]
Total						$1.6\text{-}1.8*10^9$	$1.7*10^9$	taking Fe-mn flux as calculated by [3]	0.92-2.46	1.54	
						$6.3\text{-}8.5*10^8$	$7.2*10^8$	taking Fe-mn flux as calculated by [10]	0.94-1.99	1.47	

*1, Bruland and Lohan (2003); 2, Cameron and Vance (2014); 3, Takano et al. (2017); 4, Jickells et al. (2005); 5, Rudnick and Gao (2014); 6, Desboeufs et al. (2005); 7, Cameron et al. (2009); 8, Gall et al. (2013); 9, Hedges and Keil (1995); 10, Vance et al. (2016); 11, Little et al. (2015).

[1]Obtained using the average authigenic δ^{60}Ni for Peru Margin sediments.

[2]Using the Lagoa Salgada OPF samples.

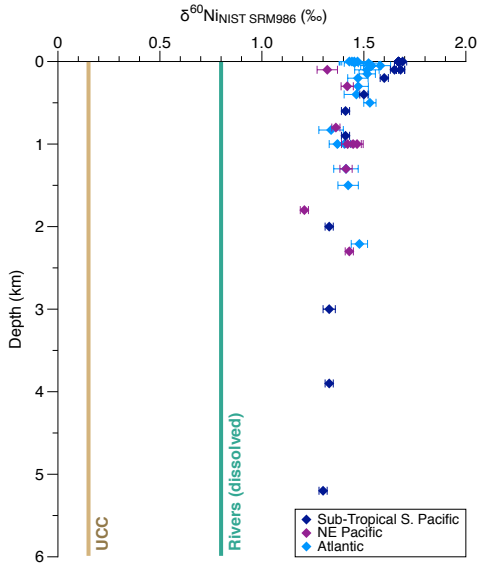

Figure 1: Published Ni isotope data for seawater compared to that of the discharge weighted average for the dissolved phase of rivers (turquoise line) and to that of the upper continental crust (UCC, brown line). Data from Cameron and Vance (2014) and Takano et al. (2017).

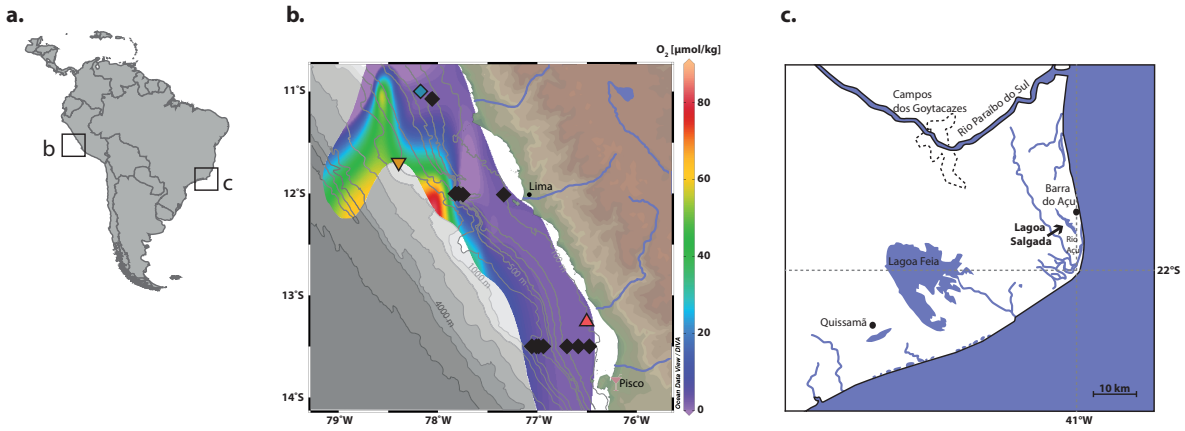

Figure 2: Map of sample provenance (a). Details of the Peru margin setting (b) where core-top samples (black diamonds) and three down-core profiles (colorful symbols) were taken. Grey shading indicates bathymetry whereas colors indicate bottom water oxygen. Oxygen data from CTD casts was gridded in ODV with DIVA scaling. Details of the Lagoa Salgada setting (c) modified from Birgel et al. (2015).

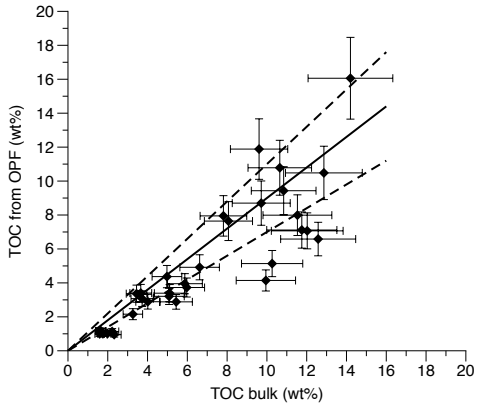

Figure 3: TOC data for the bulk samples, measured before any HF-HCl treatment, plotted versus the TOC content of the OPF, obtained after the HF-HCl digestion. Plotted error bars reflect the repeatability of standards and samples and are ±15% (relative). Most data fall on an array (solid line, slope = 0.9) that implies 90% retention of the organic carbon in the OPF after the HF digestion. The dashed lines bracket nearly all the data and have slopes of 0.6 and 1.2.

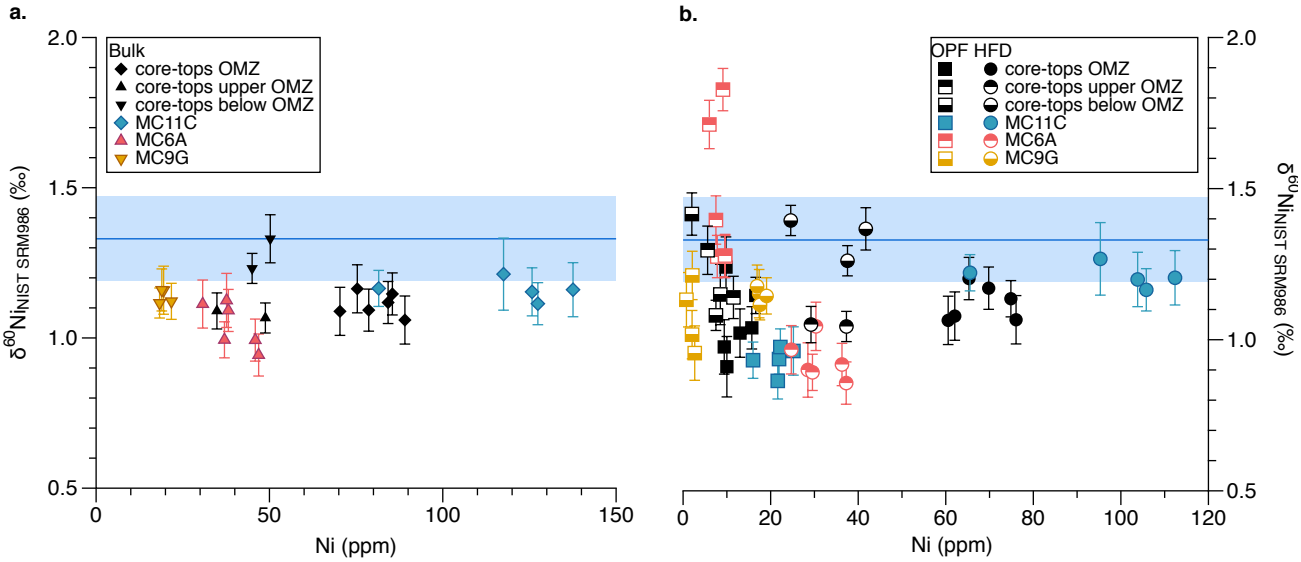

Figure 4: Peru margin Ni abundances and isotope composition calculated for bulk samples (a) and as measured for the respective OPF and HFD fractions of the same samples (b). The blue line and associated band indicate the average and 2σ of the Ni isotopic composition of the modern deep ocean (defined by depths greater than 1000m, references in text).

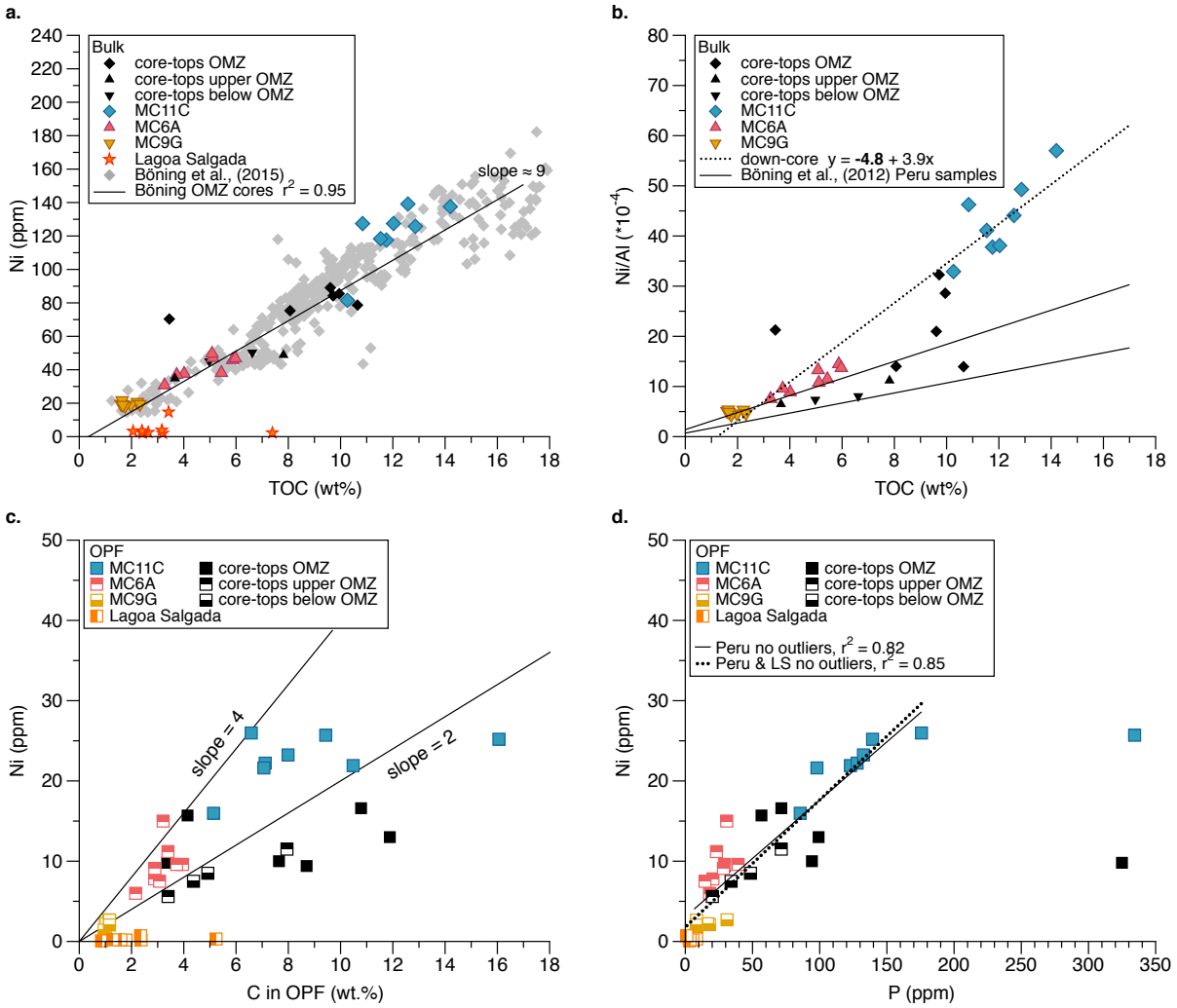

Figure 5: Ni abundances plotted versus TOC for the sediments studied here. (a) Data for Peru Margin bulk sediments, compared to data reported in Böning et al. (2015) for sediments in upwelling regions globally. The strong correlation between Ni abundance and TOC in the OMZ sediments suggests delivery of Ni to the sediments via organic matter (data in gray from Böning et al., 2015). (b) Ni/Al vs. TOC for the Peru Margin sediments studied here. The Ni organic matter association for Peru margin samples is further supported by (c) the correlation between Ni abundance in the OPF fraction versus %orgC in the OPF and (d) the strong correlation between Ni and P abundances in the OPF fraction in all but two of the Peru Margin samples.

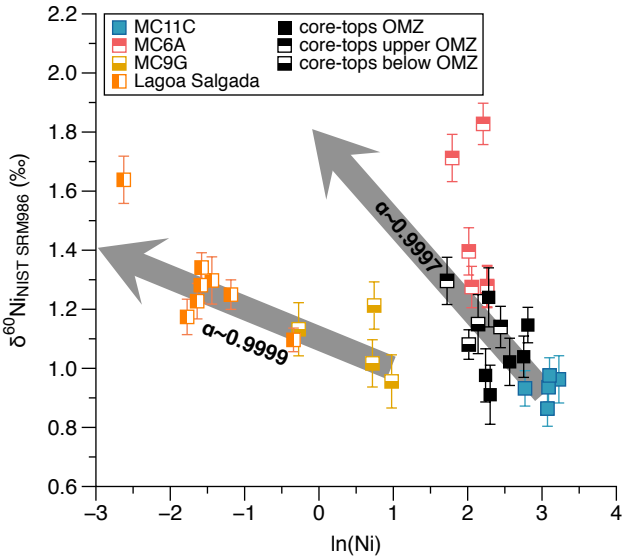

Figure 6: δ^{60}Ni vs. ln[Ni] in the organic-pyrite fractions (OPF) of Peru Margin and Lagoa Salgada sediments. Most Peru Margin samples for cores within the OMZ, as well as all core-top samples, lie on an array that is consistent with removal of Ni from a water column with a Ni isotopic composition close to the deep ocean value. The arrow labeled $\alpha = 0.9997$ shows the expected array if the Ni in the OPF is derived from the photic zone with preferential removal of the light isotope as observed in the water column (Archer et al., 2017; Takano et al., 2017). Most of the data for the Peru Margin samples are consistent with this process. Data for both the Peru Margin core from beneath the OMZ and the Lagoa Salgada may define a fractionation trend representing an alpha that is closer to 1.

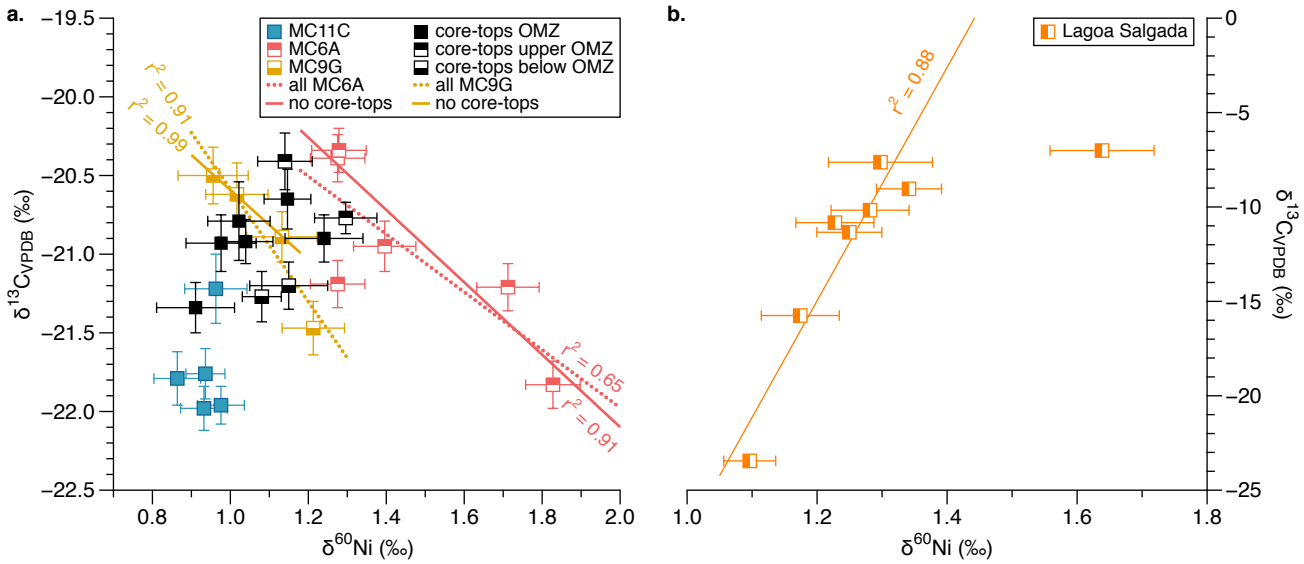

Figure 7: δ^{60}Ni vs. δ^{13}C. Peru margin down-core sediments from the upper edge of and below the OMZ show inverse correlations between δ^{60}Ni and δ^{13}C of the OPF fraction that appear to be specific to each location. (b) Lagoa Salgada OPF fractions exhibit an opposite (positive) correlation between δ^{60}Ni and δ^{13}C.

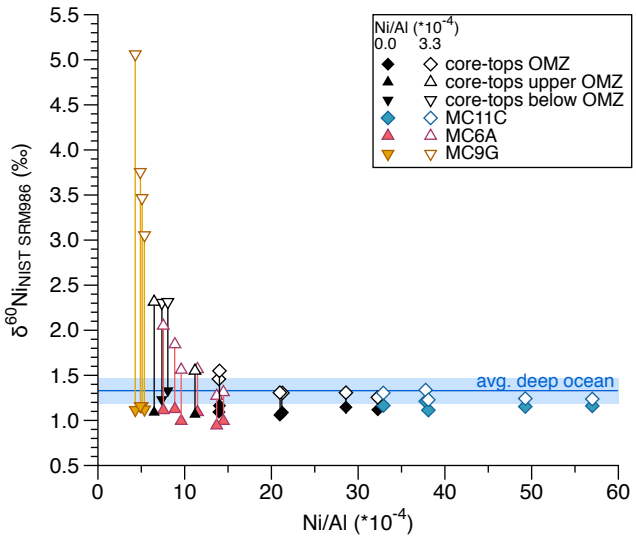

Figure 8: Peru Margin authigenic δ^{60}Ni obtained after a correction for detrital Ni, using Ni/Al detrital of 0 (i.e., no correction, filled symbols) and of 3.3*10^{-4} g/g (empty symbols). The bars between the empty and filled symbol of each sample indicate the range along which the $\delta^{60}\text{Ni}_{\text{authigenic}}$ could lie. The blue line and associated band indicate the average and 2σ of the Ni isotopic composition of the modern deep ocean (defined by depths greater than 1000m, references in text).

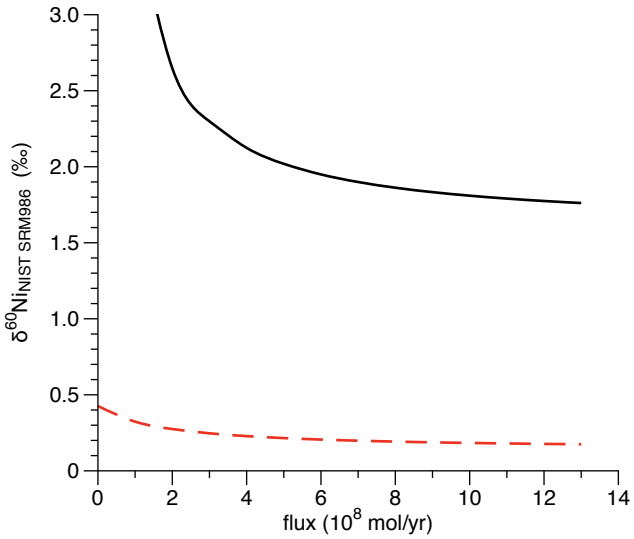

Figure 9: Requirements of two alternative ways to balance the oceanic budget of Ni and its isotopes. The black curve shows the required isotope composition of a projected missing input versus its size, given a range in size of the Fe-Mn oxide output from that required to balance the currently known inputs (missing input = zero) up to $1.5*10^9$ mol/yr (Cameron and Vance, 2014). The δ^{60}Ni of the Fe-Mn oxide output is taken to be the average of data in Gall et al. (2013). The red curve assumes that the required missing input has an isotope composition the same as the upper continental crust, and explores the δ^{60}Ni of the effective – e.g. final buried - Fe-Mn oxide output following potential diagenetic modification. Other parameters, for the size and isotopic composition of the better known inputs and outputs, as summarized in Table 3.

Electronic Supplementary Material

S1. Peru Margin sample locations and details

Table S1: Peru margin sediment core locations

core ID	lat/long [°N/°E]	depth [m]	bottom O_2 [μM]	location wrt OMZ
R/V Seward Johnson 10-92				
BC39	-13.509 / -76.927	550	10	within OMZ
BC57	-13.512 / -76.695	172	<10	within OMZ
BC62	-13.499 / -76.959	643	10	below OMZ
BC76	-13.502 / -76.983	725	15	below OMZ
BC81	-13.508 / -76.578	130	10	within OMZ
KC83	-13.518 / -76.473	106	10	upper OMZ
BC93	-12.000 / -77.335	100	5	upper OMZ
BC125	-11.998 / -77.807	340	5	within OMZ
KC127	-11.996 / -77.790	309	5	within OMZ
BC153	-11.062 / -78.073	250	5	within OMZ
R/V Knorr 182-9				
MC6A	-13.250 / -76.500	100	2	upper OMZ
MC9G	-11.718 / -78.399	1500	80	below OMZ
MC11C	-11.000 / -78.167	325	2	within OMZ

S2. Analytical Methods

S2.1. General analytical procedure

All procedural steps described in this study were performed in the clean laboratory facilities at the Institute of Geochemistry and Petrology at ETH Zürich. All containers used were trace metal cleaned Savillex PFA labware products and all acids were either of ultrapure grade or twice distilled before use.

The HF-digestible fraction was obtained via a HF-HCl digestion of ∼1g of sediment performed in 60ml Teflon beakers. Specifically, this involves a 24hr digestion at 150°C in 3ml concentrated HF and 2ml of 7M HCl mixture, followed by two steps involving 24hr reflux at 150°C with 7M HCl, evaporating to dryness between each step. 7M HCl is then added a final time, again refluxing 24hr at 150°C. The resulting HF-dissolvable fraction (HFD) and the residual solid (organic matter and associated pyrite, OPF) were then separated by centrifugation and decanting of the supernatant solution. The residual OPF was brought into solution via high-pressure ashing (HPA-S by Anton Paar) in a 10:1 mixture by volume of 13M HNO_3 and 10M HCl, subsequent evaporation to dryness, and final dissolution in 1ml of 0.3M HNO_3.

All OPF and HFD fractions were analyzed for elemental abundances on a ThermoScientific Element XR^{TM} inductively-coupled plasma mass spectrometer (ICP-MS) at ETH Zürich. Accuracy and reproducibility were determined by repeat analyses of a commercially available carbonate-enriched shale standard (Green River Shale, SGR-1, United States Geological Survey, USA). For Ni and Al the long-term reproducibility of this standard, assessed over the period during which the data here presented were obtained, is ±8% and ±7% (2SD, n = 40), respectively, and the measured concentrations are, for both, 100% of their certified values.

For isolation and purification of Ni fractions from other elements and from the sam-

ple matrix, a sample aliquot containing approximately 100ng of Ni was first spiked with a ^{61}Ni-^{62}Ni double spike and the mixture allowed to equilibrate for up to 24hr. Spiked samples were then passed through an anion exchange column (Bio-Rad macroporous AG MP-1M resin) and a subsequent column filled with Ni-specific DMG resin (Eichrom Technologies) following the procedure outlined in Cameron and Vance (2014). Oxidation for 3 - 5 days was then necessary to remove Ni-bound DMG. At this point we noted that some samples still contained elevated amounts of Ca relative to Ni. This resulted in an interference at mass 56 (^{40}Ca^{16}O), which we use to monitor a potential ^{58}Fe interference on ^{58}Ni (see below), so that we introduced an additional Nobias-chelate PA1 (Hitachi High Technologies) column prior to the final anion exchange column step described in Cameron and Vance (2014). The additional Nobias-chelate PA1 resin column is a miniaturized, gravity-driven version of the large flow-through system described by Takano et al. (2013) for processing of seawater samples. The columns, containing the Nobias-chelating PA1 resin, were cleaned with 1ml 1M HCl, and conditioned with 1ml MQ H_2O followed by two passes of 0.5ml 30mM $AcNH_4$ buffer. The sample, following oxidation to remove Ni-bound DMG, is dissolved in a 10:1 mixture of 0.5M HCl and 1M ammonium acetate buffer, with pH adjusted to 5 ± 0.5 by addition of ammonia solution. The matrix is eluted in 0.5ml 30mM AcNH4 buffer, and the Ni fraction is collected in 1ml of 1M HCl. A final anion exchange column is used to remove any residual Fe. The total Ni blank for this procedure was 3ng, dominated by the DMG column. A blank correction was applied to all samples assuming a δ^{60}Ni for the blank of 0‰. For all except one sample, the resulting shift is no greater than analytical uncertainty (for LS30 OPF δ^{60}Ni is shifted upwards by 0.15‰ relative to that with no blank correction). Alongside each set of samples passed through the entire column procedure described above, we also process one of two USGS Fe-Mn nodule standards (Nod A1 and Nod P1).

Isotopic analyses of ∼100 ppb of the purified Ni fractions, dissolved in a solution of 0.3M HNO_3, were performed using a ThermoFinnigan NeptunePlus multicollector ICPMS at ETH Zürich. The sample introduction system comprised either a CPI PFA nebulizer

834 (50μl/min) or a Savillex C-Flow PFA nebulizer (35 or 50μl/min) connected to an Aridus.
835 A known interference from ^{58}Fe on ^{58}Ni was monitored by measuring ^{56}Fe and applying a
836 correction. Many of the samples in this study had small residual amounts of Fe in the Ni
837 fraction, in most cases blank Fe from the small anion column at the end of the chemical
838 separation procedure. An interference-correction for ^{58}Fe on ^{58}Ni was tested by analyzing
839 Fe-doped Ni standard-spike mixtures. The results of this test are shown below (Fig. S1)
840 for a range of measured 56/58 signal ratios up to values in excess of 20. Ratios in the
841 samples reported here were almost all <0.3, but six Lagoa Salgada OPF samples were in
842 the range 0.3-0.7 and one was 2.6. Correction for mass discrimination was done using the
843 double spike approach, as detailed in Cameron and Vance (2014).
844
845

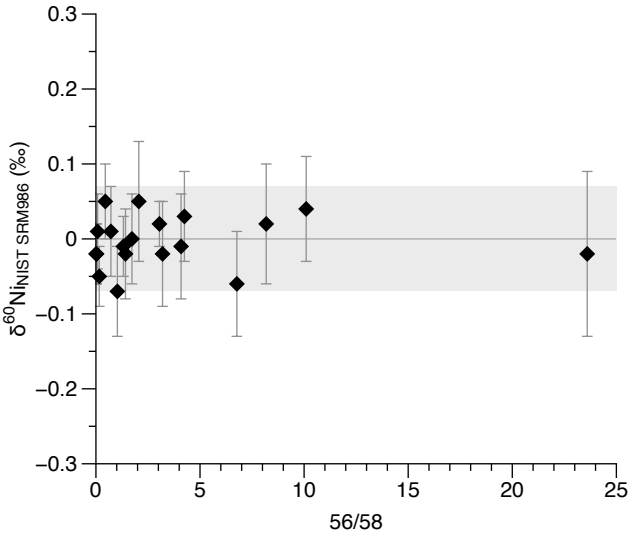

Figure S1: δ^{60}Ni for Fe-doped spike-NIST standard mixtures (expected result = 0‰, average and 2SD of all data = 0.00 ± 0.07 ‰, gray band). These data were obtained in two analytical sessions. To verify that the correction is robust over long periods, all subsequent sessions contained a measurement of an Fe-doped standard-spike mixture with a 56/58 ratio of 2 - 3. That the measured 56 signal is ^{56}Fe is verified through measurement of the 56/57 ratio. The required ^{58}Fe/^{56}Fe ratio for the correction to be successful for standards was 0.003087 and a mass bias was applied to this ratio using the measured versus mass-bias corrected ^{60}Ni/^{58}Ni ratio for pure NIST standards measured at the start of each analytical session.

The internal error is determined by propagation of the uncertainties obtained from the NeptunePlus analysis through the double spike algebra. The long-term external reproducibility was determined by repeat measurements of two secondary standards, USGS NodA1 and Nod P1. Analyses performed during the period when the data presented here were obtained yielded $\delta^{60}\mathrm{Ni} = 1.04 \pm 0.07$ ‰ (n = 120) and $\delta^{60}\mathrm{Ni} = 0.34 \pm 0.08$ ‰ (n=99), respectively. In all tables and diagrams, these reproducibilities are taken to be the real uncertainties unless, as in rare cases when analytical signals were small, the internal uncertainty was greater, in which case the latter is used.

Freeze-dried sediment samples and the extracted OPFs were analyzed for total organic carbon (TOC) and for their $\delta^{13}\mathrm{C}$ composition using a ThermoFisher Flash-EA 1112 via a Conflo IV interface to a ThermoFisher Delta V isotope ratio mass spectrometer (IRMS), with a long-term reproducibility of 5 - 15%. The freeze-dried bulk sediments were first decarbonated with 6M HCl for 24hr, rinsed with MilliQ and then dried at 50°C for at least 48hr. All samples were combusted in an oxidation column at 1020°C. Combustion gases were passed through a reduction column set at 650°C, the resulting N_2 and CO_2 gases were separated chromatographically and transferred to the IRMS via an open split for on-line isotope measurements.

S2.2. Tests of digestion approach

We examined the OPF fractions using SEM (e.g., Fig. S2). The dominant visible fraction is organic material as confirmed by semi-quantitative *in situ* EDAX analyses, but there are also, clearly, bright cuboid grains that are identified as sulphide. At this stage we do not know the Ni mass balance between these two phases.

As summarized briefly in section 3.1 of the main paper, we also investigated potential method-induced isotope fractionation by subjecting three sub-samples of a single core-top (BC81) to one, two, and three digestions. The OPF was obtained and analyzed only at the end of these sets of HF extractions. The approach is shown schematically in Figure

S3. Each of the three subsamples A, B, and C were processed in duplicate. The resulting Ni concentration and isotope composition for each HFD and OPF fraction are reported in Table S1. In all cases most of the nickel in the HFD fraction is recovered during the first digestion, with only minor contributions from a second and third digestion (Fig. S4). The nickel isotope composition of the HFD fractions are within analytical uncertainty of each other (Fig. S5) except for the very small amount of Ni in fraction HFD3 from sub-sample C, a substantial portion of which is certainly blank. The Ni concentrations and isotopic compositions of the three OPF fractions are also practically identical within analytical uncertainties (Fig S4, 5). After this test, all samples processed in this study were digested only once. This experiment suggests that a single extraction accesses almost all the HF-extractable Ni, and that the OPF is not significantly affected by the HF extraction – e.g., there is no difference in either concentration or δ^{60}Ni after one, two or three HF extractions.

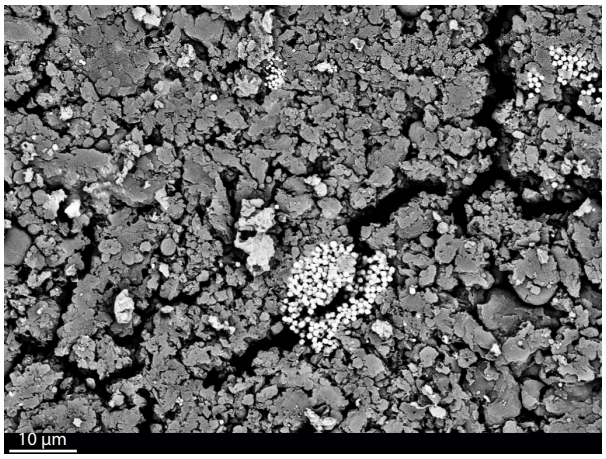

Figure S2

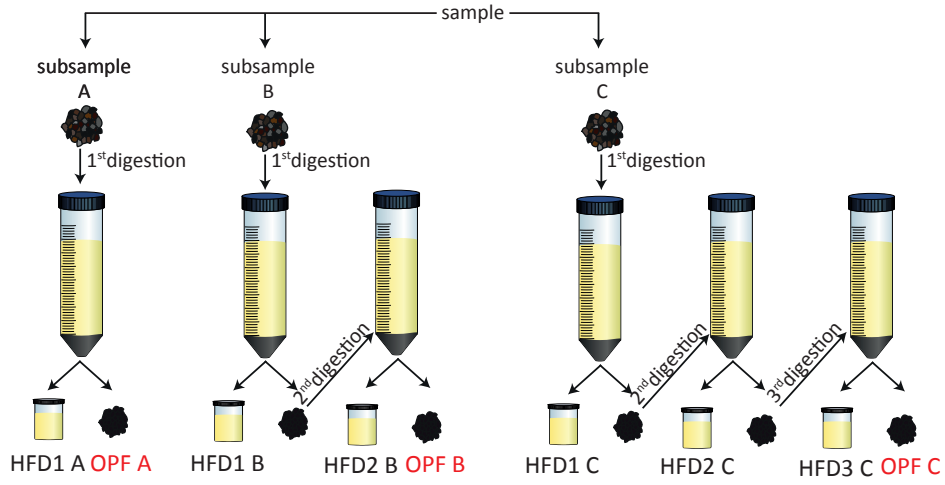

Figure S3: Schematic representation of the method validation experiment. All subsample digestions were repeated in complete duplicate but only one of each is shown here.

Table S2: Results of method validation experiments

sample	duplicate 1			duplicate 2			average		
	Ni Elem[1] [ppm]	δ^{60}Ni [‰]	2σ	Ni Elem[1] [ppm]	δ^{60}Ni [‰]	2σ	Ni Elem[1] [ppm]	δ^{60}Ni [‰]	2σ[2]
BC81A OPF	12	1.21	0.06	16	1.16	0.06	14	1.19	0.07
BC81A HFD1	104	1.33	0.05	119	1.28	0.03	111	1.30	0.07
BC81B OPF	12	1.04	0.04	13	1.06	0.03	12	1.05	0.07
BC81B HFD1	119	1.31	0.04	117	1.23	0.04	118	1.27	0.07
BC81B HFD2	10	1.21	0.04	7.5	1.31	0.07	8.8	1.26	0.07
BC81C OPF	12	1.03	0.03	8.7	1.00	0.02	10	1.01	0.07
BC81C HFD1	67*	1.26	0.04	110	1.31	0.04	110	1.28	0.07
BC81C HFD2	8.9	1.19	0.07	14	1.18	0.05	12	1.18	0.07
BC81C HFD3	2.7	1.02	0.04	2.9	n/a	n/a	2.8	1.02	0.07

[1] Concentrations obtained via ElementXR analysis.

[2]All duplicate analyses agree to a level that is consistent with the long-term reproducibility and this is used as the uncertainty here and in Fig. S5.

*Leakage of solution from beaker, hence this concentration was not used in the calculation of the average.

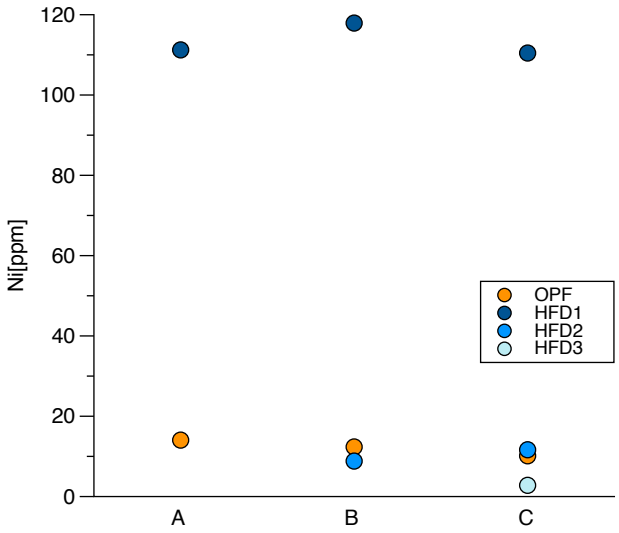

Figure S4: Ni concentrations in the OPF and HFDs for each of the three method validation steps. Note that most of the Ni in the HFD fraction is recovered with the first digestion, with contributions from further digestion being minor.

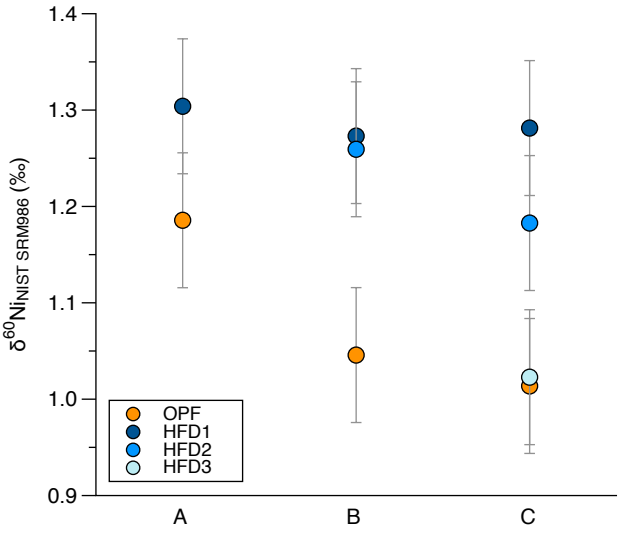

Figure S5: Ni isotope composition of the OPF and HFDs for each of the three method validation steps. Error bars indicate the long-term external reproducibility (2σ).

A separate issue concerns the presence of small amounts of residual Al in the OPF, and the degree to which the OPF may contain residual undigested clays. Table S3 presents

890 further data for the chemistry of the OPF. Elemental ratios do not correspond to those of
891 clays. They *do* correspond to those of fluoride salts that are commonly residual after HF
892 digestion of silicates (e.g., Croudace, 1980). Powder XRD analyses on two OPF fractions
893 (Figure S6) confirm the presence of fluorides in the OPF, hence likely explaining the
894 presence of Al in the OPF.

Table S3: Elemental abundance and ratios to Al of Na, Mg, Ca in OPF

sample	Na (wt.%)	Mg (ppm)	Ca (ppm)	Al (wt.%)	Na/Al	Mg/Al	Ca/Al
BC39	1.4	2901	6223	1.0	1.4	0.28	0.60
BC57	3.9	3112	2197	0.7	5.3	0.42	0.30
BC62	1.8	2882	4555	0.9	2.0	0.32	0.50
BC76	3.0	5982	9089	1.5	2.1	0.41	0.62
BC81	4.2	3658	1043	1.1	3.7	0.32	0.09
KC83	5.8	4663	1203	1.3	4.3	0.35	0.09
BC93	3.9	2053	812	0.3	12	0.65	0.26
BC125	4.3	2561	2103	0.7	6.3	0.38	0.31
KC127	4.5	2490	2119	0.4	11	0.61	0.52
BC153	3.1	1314	1762	0.1	22	0.93	1.2
MC6A1	3.2	3717	1179	0.7	4.7	0.54	0.17
MC6A6	2.8	4548	923	0.8	3.4	0.55	0.11
MC6A14	2.5	4394	1166	0.9	2.9	0.52	0.14
MC6A16	2.3	5149	1785	1.1	2.1	0.47	0.16
MC6A22	1.0	3994	1159	0.9	1.2	0.47	0.14
MC6A26	1.2	4423	1783	1.2	1.1	0.38	0.15
MC6A37	1.1	2357	558	0.5	2.2	0.46	0.11
MC6A4446	1.1	3066	1033	0.8	1.2	0.36	0.12
MC9G1	0.6	3042	7643	0.4	1.5	0.74	1.9
MC9G3	0.6	2937	9162	0.4	1.6	0.79	2.5
MC9G5	0.5	3257	8020	0.4	1.1	0.80	2.0
MC9G7	0.2	1215	2491	0.2	1.0	0.53	1.1
MC9G9	0.5	1406	7188	0.4	1.4	0.39	2.0
MC9G11	0.5	2731	9244	0.3	1.4	0.78	2.7
MC9G13	0.4	3128	7729	0.4	1.0	0.80	2.0
MC11C4	2.7	4696	1753	0.7	3.7	0.64	0.24
MC11C8	1.7	4239	2228	0.7	2.4	0.59	0.31
MC11C17	1.3	5162	2093	0.9	1.4	0.55	0.22
MC11C23	1.3	4516	2632	0.8	1.7	0.56	0.33
MC11C28	0.6	3647	1721	0.7	0.8	0.52	0.24
MC11C35	0.2	1716	1345	0.3	0.8	0.54	0.42
MC11C37	0.7	3902	1827	0.9	0.7	0.44	0.21
MC11C4648	0.7	4737	12823	1.0	0.7	0.45	1.2
LS14	0.8	209	1526	0.04	23	0.59	4.3
LS20	0.8	852	1302	0.1	7.3	0.82	1.3
LS25	1.0	1771	3050	0.2	6.3	1.1	1.9
LS30	0.3	1893	4949	0.2	1.3	0.86	2.3
LS35	0.4	4110	5163	0.4	1.1	1.1	1.4
LS40	0.6	4274	6112	0.4	1.4	1.0	1.5
LS45	0.3	1053	1288	0.1	2.7	0.93	1.1
LS65	0.6	6964	20390	1.1	0.5	0.62	1.8

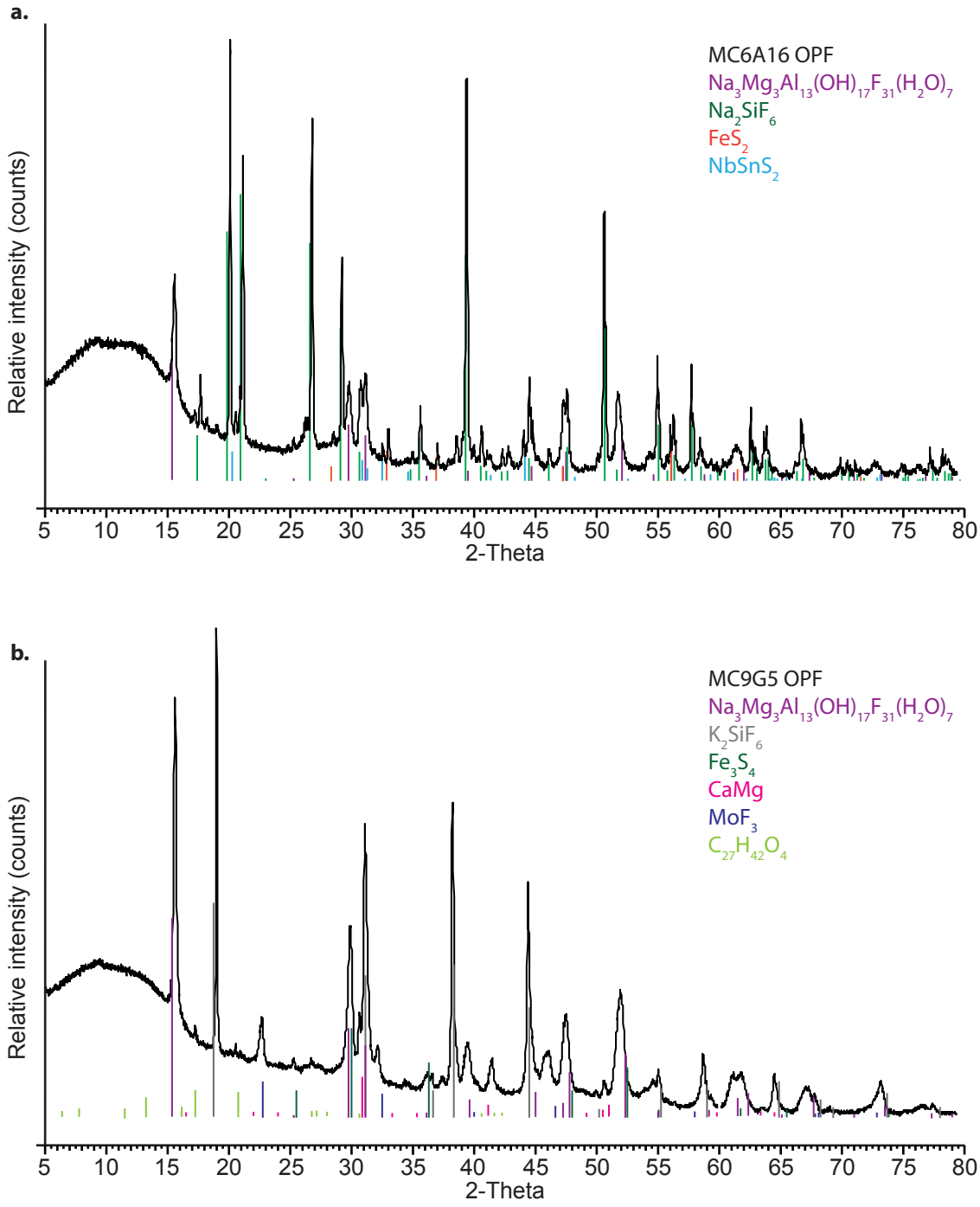

Figure S6: Powder XRD profiles for two OPF fractions (samples MC6A16 OPF and MC9G5 OPF).

S3. Mass Balance: Hydrothermal sources of Ni

As stated in the main text, the impact of hydrothermal processes on the oceanic budget has not thus far been quantified – whether they represent an input, an output, what the isotopic effects associated with them are. Water column data in the vicinity of the mid-Atlantic Ridge (Fig. S7), that clearly highlight a source of Fe from the ridge, do not show any similarly anomalous Ni concentrations. Indeed, Ni concentrations are, if anything, lightly lower in the Fe plume suggesting removal of Ni, possibly by scavenging to Fe-rich particulates.

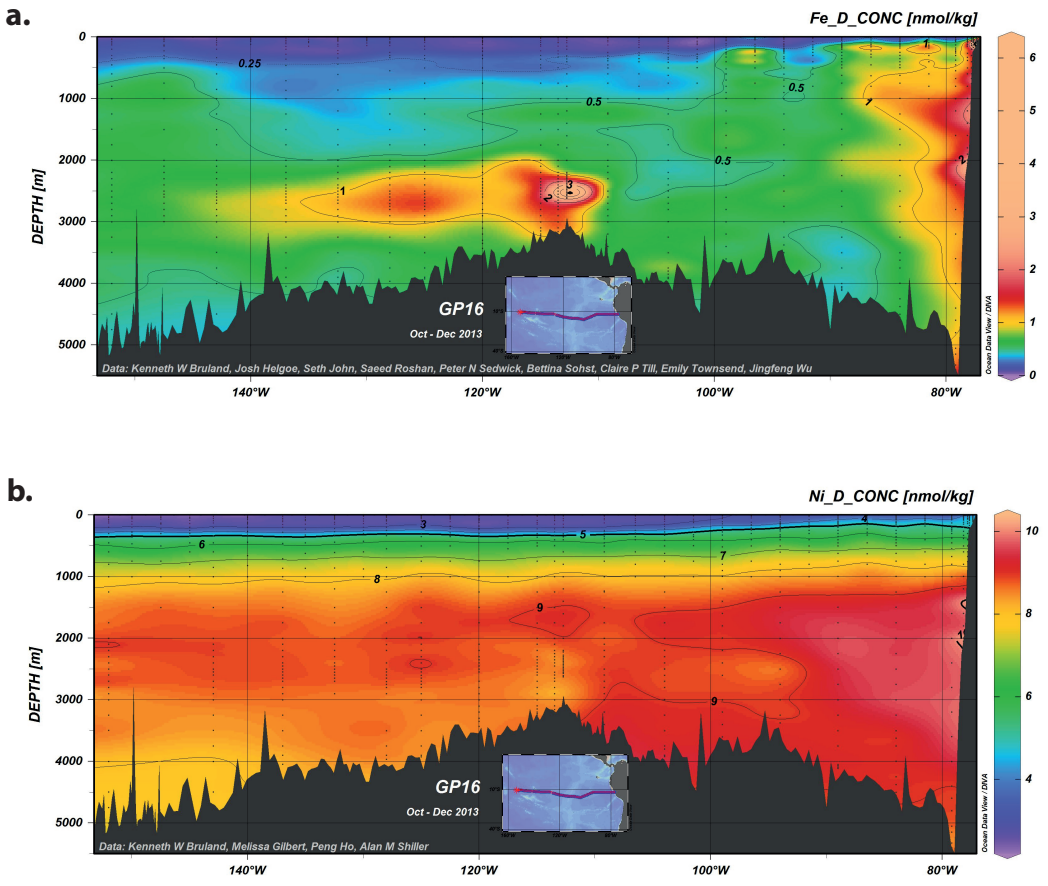

Figure S7: Comparison of dissolved Fe (a) and dissolved Ni (b) concentrations along the GEOTRACES transect GP16 that crosses the Mid-Atlantic Ridge. Plots from the eGEOTRACES Electronic Atlas based on data from the IDP2017 (Schlitzer, 2017).

References

Cameron, V., Vance, D., 2014. Heavy nickel isotope compositions in rivers and the oceans. Geochimica et Cosmochimica Acta 128, 195–211.

Croudace, I. W., Jan. 1980. A possible error source in silicate wet-chemistry caused by insoluble fluorides. Chemical Geology 31, 153–155.

Schlitzer, R., 2017. eGEOTRACES - Electronic Atlas of GEOTRACES Sections and Animated 3d Scenes. http://www.egeotraces.org.

Takano, S., Tanimizu, M., Hirata, T., Sohrin, Y., 2013. Determination of isotopic composition of dissolved copper in seawater by multi-collector inductively coupled plasma mass spectrometry after pre-concentration using an ethylenediaminetriacetic acid chelating resin. Analytica Chimica Acta 784, 33–41.